Chapter 23
Electricity-to-Light Conversion

Abstract Light emitting diodes (LEDs) and laser diodes are the focus of this chapter. For LEDs materials choices, the concepts of internal and external quantum efficiency as well as device design are treated. Special devices such as white LEDs, quantum dot and organic LEDs are introduced. For laser diodes the concepts of gain, loss and threshold, various heterostructures for modern device design and laser emission properties such as mode spectrum, far field, dynamics and tunability are discussed. Finally special devices such as the hot hole laser, the cascade laser and semiconductor optical amplifiers are mentioned.

23.1 Radiometric and Photometric Quantities

23.1.1 Radiometric Quantities

The radiometric quantities are derived from the radiant flux (power) Φ_e (or usually simply Φ) that is the total power (energy per time) emitted by a source, measured in Watts. The radiant intensity I_e is the radiant flux emitted by a point source into a solid angle,[1] measured in Watts per steradian (or W/sr). The irradiance E_e is the radiant flux per area incident on a given plane, measured in W/m^2. The radiance L_e is the radiant flux per area and solid angle as, e.g., emitted by an extended source, measured in W/(m^2 sr).

23.1.2 Photometric Quantities

The photometric quantities are related to the visual impression and are derived from the radiometric quantities by weighting them with the $V(\lambda)$ curve.

---

[1] A solid angle Ω is the ratio of the spherical surface area A and the square of the sphere's radius r, i.e. $\Omega = A/r^2$.

M. Grundmann, *The Physics of Semiconductors*, Graduate Texts in Physics,
DOI 10.1007/978-3-319-23880-7_23

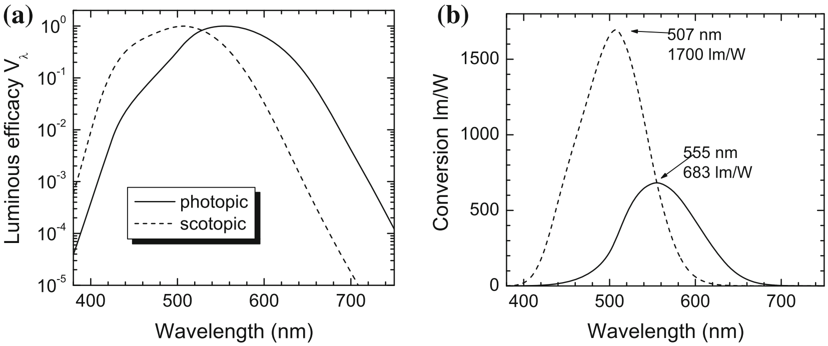

Fig. 23.1 (**a**) Relative eye sensitivity curves for photopic (light adapted, *solid line*) and (dark adapted, *dashed line*) vision. (**b**) Conversion of lumen to Watt for light- and dark-adapted vision

The luminous flux (luminosity or visible brightness) Φ_v of a source with the radiant flux (spectral power distribution) $\Phi(\lambda)$ is given by

$$\Phi_\mathrm{v} = K_\mathrm{m} \int_0^\infty \Phi(\lambda)\, V(\lambda)\, \mathrm{d}\lambda, \tag{23.1}$$

with $K_\mathrm{m} = 683\,\mathrm{lm/W}$. This formula is also the definition of the unit 'lumen'. In Fig. 23.1b, the conversion function[2] $V(\lambda)$ is shown for light and dark adapted vision.[3]

Further derived photometric quantities are luminous intensity (luminous flux per solid angle), measured in candela (cd), the illuminance (luminous flux per area), measured in lux (lx), and the luminance (luminous flux per area and solid angle). The latter is particularly important if the radiation enters an optical system, e.g. for refocusing. The radiometric and photometric quantities are summarized in Table 23.1.

---

[2] The $V(\lambda)$ curve has been experimentally determined by letting several observers adjust (decrease) the perceived brightness of a monochromatic light source at 555 nm to that of light sources of the same absolute radiation power at other wavelengths with so-called heterochromatic flicker photometry. The 'relative sensitivity curve for the CIE Standard Observer' was determined in 1924. The 'standard observer' is neither a real observer nor an average human observer. The curve has shortcomings, e.g., due to the used spectral band width (20–30 nm) of the light sources and the comparison of spectral power instead of the photon flux.

[3] While photopic vision is due to cones, the scotopic (dark-adapted) vision is due to rods. Rods are more than one thousand times as sensitive as the cones and can reportedly be triggered by individual photons under optimal conditions. Rods predominate in the peripheral vision and are not color sensitive.

Table 23.1 Radiometric and photometric quantities and units

Radiometric			Photometric		
Quantity	Symbol	Unit	Quantity	Symbol	Unit
Radiant flux	Φ_e	W	Luminous flux	Φ_v	lm
Radiant intensity	I_e	W/sr	Luminous intensity	I_v	cd
Irradiance	E_e	$\mathrm{W/m^2}$	Illuminance	E_v	lx
Radiance	L_e	$\mathrm{W/m^2/sr}$	Luminance	L_v	$\mathrm{lm/m^2/sr}$

The photometric units are lumen (lm), lux ($\mathrm{lx} = \mathrm{lm/m^2}$) and candela ($\mathrm{cd} = \mathrm{lm/sr}$)

23.2 Scintillators

A scintillator (or phosphor) is a material that converts impacting high-energy radiation into photons [1628]. Besides a high conversion efficiency, the spectrum and decay time constant of the scintillator are important for display applications. For display purposes, the photons are directly used for forming the image for the observer. For radiation detection, the photons are fed to a photomultiplier tube and counted.

The most prominent applications, involving the conversion of electrons, are the screens of cathode ray tubes (CRT) (acceleration voltage $>10\,\mathrm{kV}$) and of flat panel devices, such as field-effect displays (using a low voltage for excitation, typically $<1\,\mathrm{kV}$) or plasma displays (using the UV light from the discharge of a plasma placed between two electrodes for excitation). Further details on electroluminescent displays can be found in [1629]. Other forms of radiation detected with scintillators are α-, β-, and γ-radiation, X-rays and neutrons [1630]. Different excitation conditions require different phosphors for optimal performance.

23.2.1 CIE Chromaticity Diagram

The CIE[4] procedure converts the spectral power distribution (SPD) of light from an object into a brightness parameter Y and two chromaticity coordinates x and y. The chromaticity coordinates map the color[5] with respect to hue and saturation on the two-dimensional CIE chromaticity diagram. The procedure for obtaining the chromaticity coordinates for a given colored object involves determination of its

---

[4] Commission Internationale de l'Éclairage. The color space can be described by different coordinate systems, and the three most widely used color systems, Munsell, Ostwald, and CIE, describe the color space with different parameters. The Munsell system uses hue, value, and chroma and the Ostwald system uses dominant wavelength, purity, and luminance. The more precise CIE system uses a parameter Y to measure brightness and parameters x and y to specify the chromaticity that covers the properties hue and saturation on a two-dimensional chromaticity diagram.

[5] This definition is motivated by the color vision of the eye. Two light sources will have the same color, even if they have different SPDs, when they evoke the same color impression to the human eye.

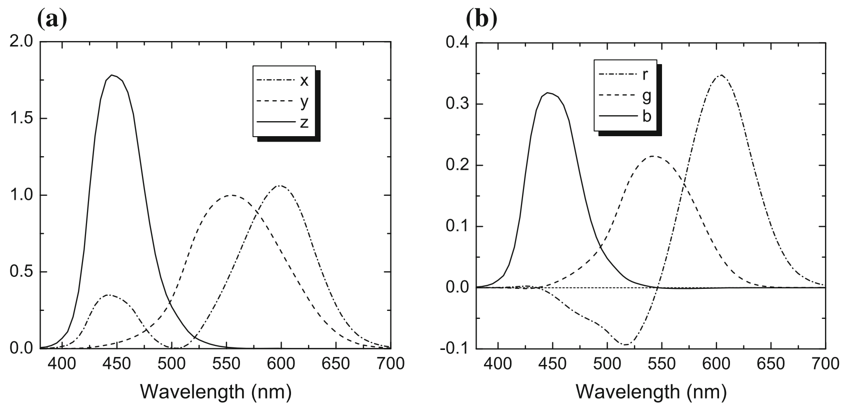

Fig. 23.2 (**a**) Color-matching functions $\bar{x}$, $\bar{y}$, and $\bar{z}$ for the calculation of the CIE chromaticity, (**b**) color-matching functions $\bar{r}$, $\bar{g}$, and $\bar{b}$ for the calculation of RGB values

spectral power distribution $P(\lambda)$ at each wavelength, multiplication by each of the three color-matching functions $\bar{x}(\lambda)$, $\bar{y}(\lambda)$, and $\bar{z}(\lambda)$ (Fig. 23.2a) and integration (or summation) of the three tristimulus values X, Y, Z

$$X = \int_{380\,\mathrm{nm}}^{780\,\mathrm{nm}} P(\lambda)\,\bar{x}(\lambda)\,\mathrm{d}\lambda \tag{23.2a}$$

$$Y = \int_{380\,\mathrm{nm}}^{780\,\mathrm{nm}} P(\lambda)\,\bar{y}(\lambda)\,\mathrm{d}\lambda \tag{23.2b}$$

$$Z = \int_{380\,\mathrm{nm}}^{780\,\mathrm{nm}} P(\lambda)\,\bar{z}(\lambda)\,\mathrm{d}\lambda. \tag{23.2c}$$

Y gives the brightness. The tristimulus values are normalized to yield the chromaticity coordinates, e.g. $x = X/(X + Y + Z)$. x and y obtained in this way are the chromaticity coordinates. The third coordinate $z = 1 - x - y$ offers no additional information and is redundant. Therefore, the color is represented in a two-dimensional diagram, the CIE chromaticity diagram[6] as shown in Fig. 23.3a. White is represented by $x = y = z = 1/3$. In order to relate the differences between colors as perceived by the human eye more closely to the geometrical distance in the chart, a revision was made (Fig. 23.3b) with new coordinates

$$u' = 4x/(-2x + 12y + 3) \tag{23.3a}$$

$$v' = 9y/(-2x + 12y + 3). \tag{23.3b}$$

---

[6] The coloring of the chart is provided for an understanding of color relationships. CRT monitors and printed materials cannot reproduce the full gamut of the color spectrum as perceived in human vision. The color areas that are shown only depict rough categories and are not precise statements of color.

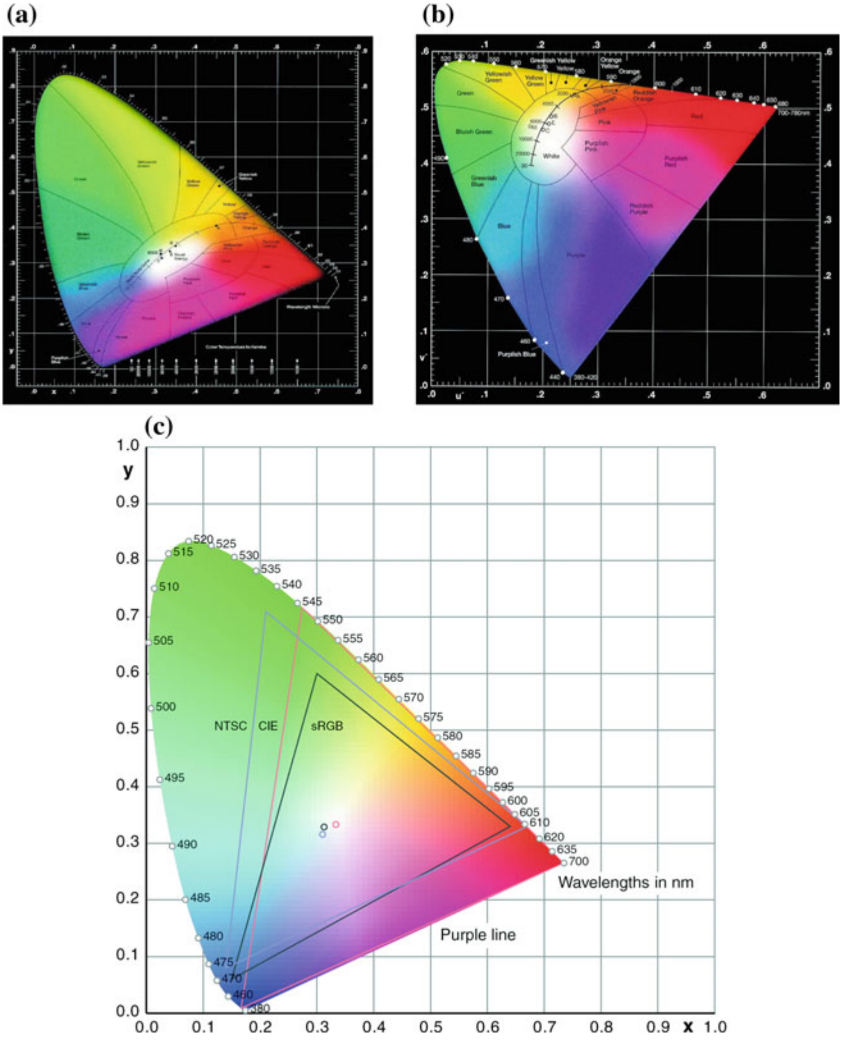

Fig. 23.3 CIE chromaticity diagram from 1931 (**a**) in the coordinates x and y and from 1976 (**b**) in the coordinates u' and v' (23.3b). The curved upper boundary is called the 'spectrum locus' and contains monochromatic colors, the straight line at the lower left is termed the 'purple boundary'. In the graph also the color of blackbody radiation is given, $T = 5440\,\text{K}$ corresponds to $x = y = 1/3$. 'A', 'B', 'C', and 'E' are standard illuminants, 'D65' denotes daylight with color temperature $T = 6500\,\text{K}$. (**c**) CIE chart with the color ranges of sRGB, CIE and NTSC. Part (**c**) adapted from [1631]

Table 23.2 Primaries and white points for sRGB, CIE and NTSC

Primary	Red		Green		Blue		White	
CIE	0.73467	0.26533	0.27376	0.71741	0.16658	0.00886	0.33333	0.33333
NTSC	0.6700	0.3300	0.2100	0.7100	0.1400	0.0800	0.3100	0.3160
sRGB	0.6400	0.3300	0.3000	0.6000	0.1500	0.0600	0.3127	0.3290

For CRTs the red-green-blue (RGB) color space is used.[7] The color matching functions for RGB values are shown in Fig. 23.2b. The RGB values are related to the XYZ values according to

$$\begin{pmatrix} R \\ G \\ B \end{pmatrix} = \begin{pmatrix} 2.36461 & -0.89654 & -0.46807 \\ -0.51517 & 1.42641 & 0.08876 \\ 0.00520 & -0.01441 & 1.00920 \end{pmatrix} \begin{pmatrix} X \\ Y \\ Z \end{pmatrix} . \tag{23.4}$$

The CIE RGB primaries from 1931 are at 700, 546.1, and 435.8 nm with the relative intensities 1.0, 4.5907, and 0.0601. A display device using three phosphors can only display colors in the triangular area of the CIE chart between the three chromaticity coordinates. For sRGB,[8] the 1931 CIE primaries and the NTSC[9] norm the coordinates are given in Table 23.2 and visualized in Fig. 23.3c. An optimal coverage of the CIE chart involves monochromatic sources (for laser TV or LED displays) at about 680, 520 and 440 nm.

23.2.2 Display Applications

The once ubiquitous amber-colored monochrome displays are mostly fabricated using ZnS:Mn [1629], having broad emission (540–680 nm) with its spectral peak at 585 nm ($x = 0.50$, $y = 0.50$) with an efficiency of 2–4 lm/W. In color television (and similar applications such as color computer monitors, tubes for aviation use, projection television) the image is reproduced by selective and time-multiplexed cathode excitation of three phosphors (blue, green and red) deposited on the internal face of the screen. The chromaticity coordinates of the standard CRT phosphors P-22B, P-22G and P-22R are given in Table 23.3. They cover about the color range

---

[7] RGB is an additive color system. However, printing devices use a subtractive color system. This means that the ink absorbs a particular color, and the visible impression stems from what is reflected (not absorbed). When inks are combined, they absorb a combination of colors, and hence the reflected colors are reduced, or subtracted. The subtractive primaries are cyan, magenta and yellow (CMY) and are related to RGB via $(C, M, Y) = (1 - R, 1 - G, 1 - B)$.

[8] Standard RGB color space as defined mainly by Hewlett-Packard and Microsoft, almost identical to PAL/SECAM European television phosphors.

[9] National television standard colors, US norm.

Table 23.3 CIE color coordinates, peak emission wavelength and decay time (10 %) of standard CRT phosphors

Phosphor	x	y	λ_p (nm)	Decay time
P-22B	0.148	0.062	440	~20 µs
P-22G	0.310	0.594	540	~60 µs
P-22R	0.661	0.332	625	1 ms

labeled 'sRGB' in Fig. 23.3c. For blue and green ZnS:Ag ($x = 0.157$, $y = 0.069$), ZnS:Ag,Cl, ZnS:Ag,Al and ZnS:Cu,Al ($x = 0.312$, $y = 0.597$), ZnS:Cu,Au,Al are used as phosphors, respectively. Y_2O_2S:Eu ($x = 0.624$, $y = 0.337$) activated with trivalent europium (Eu^{3+}) facilitated such a gain in the brilliance of red over ZnS:Ag (more than doubled it) that it has totally replaced it at about one fifth of the cost. For reproducible image quality, precise grain-size control (median size for CRT phosphors is about 8 µm), dispersion control and surface treatment are necessary. Flat-panel displays with their lower excitation voltage require different phosphors for optimal efficiency.

23.2.3 Radiation Detection

The most commonly used scintillation detector for alpha measurements is ZnS activated with silver, ZnS:Ag. This material is not very transparent to light and is usually prepared as a large number of crystals with sub-mm size attached with an adhesive to a flat piece of plastic or other material. The flat screen is optically coupled to a photomultiplier tube that is attached to associated electronics. The voltage and discriminator levels are selected so that the detector is sensitive to the rather large pulses from alpha interactions but insensitive to beta- or gamma-induced pulses. The alpha particles deposit all of their energies in a small thickness of material compared to beta and gamma radiations.

Scintillation detectors for beta radiation are often made from organic materials. In an organic scintillator, the light emission occurs as a result of fluorescence when a molecule relaxes from an excited level following excitation by energy absorption from ionizing radiation. Molecules such as anthracene, trans-stilbene, para-terphenyl, and phenyl oxazole derivatives are among the many organic species that have useful scintillation properties. The organic molecules are dissolved in organic solvents and used as liquid scintillators. A classic application is in the measurement of low-energy beta radiation from, e.g. tritium, ^{14}C, or ^{35}S. In such cases, the sample containing the radioactive beta emitter is dissolved in, or in some cases suspended in, the liquid scintillation solution. The emitted beta radiation transfers energy through the solvent to the scintillator molecule that emits light, subsequently detected by photomultiplier tubes. Organic scintillator molecules can also be dissolved in an organic monomer that can then be polymerized to produce a plastic scintillator in a wide variety of shapes and sizes. Very thin scintillators have been used for alpha detection, somewhat

Table 23.4 Emission peak wavelength and decay time of various scintillator materials

Material	λ_p (nm)	Decay time
Zn_2SiO_4:Mn	525	24 ms
ZnS:Cu	543	35–100 μs
$CdWO_4$	475	5 μs
CsI:Tl	540	1 μs
CsI:Na	425	630 ns
$Y_3Al_5O_{12}$:Ce	550	65 ns
Lu_2SiO_5:Ce	400	40 ns
$YAlO_3$:Ce	365	30 ns
ZnO:Ga	385	2 ns

thicker scintillators for beta detection. Large-volume plastic scintillators have been used in gamma detection, particularly for dose-related measurements.

Other inorganic crystalline scintillators, especially sodium iodide activated with thallium, NaI:Tl, have been used for gamma-ray energy measurements. Such detectors can be grown as large single crystals that have a reasonably high efficiency for absorbing all of the energy from incident gamma rays. There exists a rather large number of inorganic scintillators; some examples of these include cesium iodide activated with thallium, CsI:Tl, bismuth germanate, $Bi_4Ge_3O_{12}$, and barium fluoride, BaF_2. These are mostly used for gamma measurements but can also be prepared with thin windows and have been used for charged particle (e.g. alpha and beta) counting. A number of scintillator materials including tungstates like $CdWO_4$ has been reviewed in [1632].

In Table 23.4, the peak emission wavelength and the characteristic decay time are listed for a variety of scintillator materials. Direct semiconductors, although not offering the highest efficiency, are particularly useful for high time resolution in, e.g., time-of-flight measurements or fast scanning electron microscopy.

23.2.4 Luminescence Mechanisms

Self-Trapped Excitons

In a strongly ionic crystal, such as NaI, a hole becomes localized to an atomic site via the polaron effect. A spatially diffuse electron is attracted, and a self-trapped exciton is formed that can recombine radiatively.

Self-Activated Scintillator

In such material, the luminescent species is a constituent of the crystal. The emission involves an intraionic transition, e.g. 6p→6s in Bi^{3+} of $Bi_4Ge_3O_{12}$, or a charge-transfer transition in the case of $(WO_4)^{2-}$ in $CaWO_4$. At room temperature, nonradiative competing processes limit the efficiency.

Activator Ions

For dopant ions such as Eu^{2+} in YO_2S:Eu, Ce^{3+} in $YAlO_3$:Ce or Tl^{+} in NaI:Tl, the hole and electron excited by the radiation are sequentially trapped by the same ion that then undergoes a radiative transition, in the case of Eu and Ce[10] 5d→4f, for Tl $^3P_{0,1} \rightarrow S_0$. CsI:Tl has one of the highest efficiencies of 64.8 photons/keV [1633].

Core–Valence Luminescence

In some materials, e.g., BaF_2, CsF, $BaLu_2F_8$ the energy gap between the valence band and the top core band is less than the fundamental band gap. A radiative transition occurs when an electron from the valence band fills a hole in the top core band that has been created by the radiation. The light yield is limited to about 2 photons/keV.

Semiconductor Recombination Processes

Free excitons or excitons bound to impurities can recombine radiatively. This process is most efficient at low temperatures. At room temperature, the emission is typically much weaker ($\gtrsim 10\times$) since excitons become unbound or dissociated. Highly doped n-type semiconductors, e.g. CdS:In, exhibit recombination between donor-band electrons and holes. ZnO:Ga has an efficiency of about 15 photons/keV and a fast response (with 2.4 photons/keV emitted in the first 100 ps). Luminescence can also stem from donor–acceptor pair transitions, e.g. in PbI_2 with an efficiency of 3 photons/keV at 10 K. Isoelectronic impurities such as nitrogen in GaP:N and tellurium in CdS:Te attract an electron and subsequently a hole. In ZnS:Ag and ZnS:Cu (conduction) band to trap recombination is dominant. In a codoping scheme like CdS:In,Te, In supplies electrons in an impurity band that can recombine with holes trapped at Te.

23.3 Light-Emitting Diodes

23.3.1 Introduction

Light-emitting diodes (LEDs) are semiconductor devices in which injected carriers recombine radiatively. The recombination process leading to light emission can be of intrinsic nature, i.e. band–band recombination, or extrinsic, e.g. impurity-bound excitons. Impurity-related luminescence can also be excited via impact excitation. For an extensive treatment of LEDs see [1634], for a review of the early field [1635] and for recent reviews [1636, 1637]. Mostly LEDs are pn-diodes although also some MIS-based devices have been reported [1638, 1639].

---

[10] This transition is dipole allowed for Ce and partially forbidden for Eu.

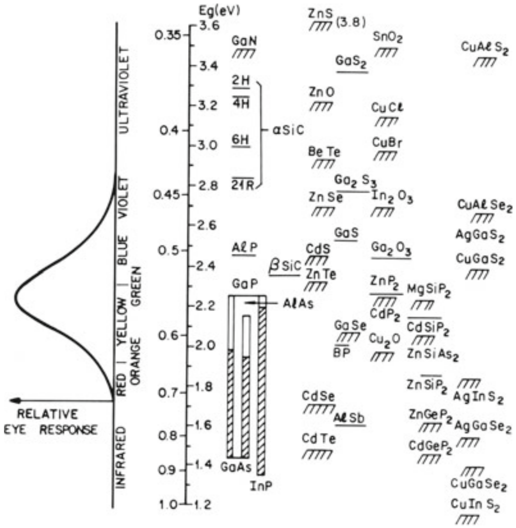

Fig. 23.4 Spectral coverage by various semiconductor materials. Reprinted with permission from [500], © 1981 Wiley

23.3.2 Spectral Ranges

Applications for LEDs can be sorted by the color of emission. In Fig. 23.4, the standard sensitivity $V(\lambda)$ of the human eye is shown (see Fig. 23.1a). In the visible spectral region (about 400–750 nm) the perceived brightness of the LED depends on the eye sensitivity. It is largest in the green (at 555 nm) and drops strongly towards the red and blue.

The most important spectral regions and applications are:

- infrared ($\lambda > 800$ nm): remote controls, optocouplers, low-cost data transmission, IR interface
- visible: indicator LED, lighting[11] (room, buildings, cars), white LED for broad spectrum
- ultraviolet ($\lambda < 400$ nm): pumping of phosphors for white LEDs, biotechnology

In Fig. 23.4, potentially useful semiconductors for the various spectral regions are shown. The semiconductors that are currently used for the various colors of the visible spectrum are

- red–yellow: Ga(As,P)/GaAs, now (Al,In,Ga)P/GaP
- yellow–green: GaAsP:N, GaP:N
- green–blue: SiC, now GaN, (In,Ga)N
- violet: GaN
- ultraviolet: (Al,Ga)N

---

[11] Penetration of white LEDs into the general lighting market could translate (globally) into cost savings of \$ 10^{11} or a reduction of power generation capacity of 120 GW.

23.3.3 *Efficiencies*

External Quantum Efficiency

The *external* (or total) quantum efficiency η_{ext} is the number of photons emitted from the device per injected electron–hole pair. It is given by the product of the *internal* quantum efficiency η_{int} and the light extraction efficiency χ_{ex}:

$$\eta_{\text{ext}} = \chi_{\text{ex}}\, \eta_{\text{int}} . \tag{23.5}$$

In a commercial device another factor, the packaging efficiency may enter which accounts for photon loss due to packaging the LED dice into its housing.

Wall-Plug Efficiency

The wall-plug efficiency η_{w} is the power conversion ratio of the electrical power and the light output P_{out},

$$\eta_{\text{w}} = \frac{P_{\text{out}}}{I\,V} = \frac{\hbar\omega}{e\,V}\, \eta_{\text{ext}} . \tag{23.6}$$

At first it seems reasonable to assume that always $\eta_{\text{w}} < 1$. However, it has been reported that at small current and at elevated temperature the wall-plug efficiency is found larger than 100 % due to the electrical work pumping heat from the lattice to the photon field in a GaSb-based diode [1640]. The groundwork for such effect was laid in [1641], essentially predicting that $\hbar\omega > e\,V$ is possible.

Internal Quantum Efficiency

The internal quantum efficiency is the number of photons generated (inside the semiconductor) per injected electron–hole pair. High material quality, low defect density and low trap concentration are important for a large value of η_{int}. The recombination current in the pn-diode is given in (21.132).

Light Extraction Efficiency

The light extraction efficiency of the LED chip is ratio of the number of photons leaving the device and the total number of generated photons.[12] The geometry of the LED is of prime importance to optimize χ_{ex}. Due to the large index of refraction of the semiconductors ($n_{\text{s}} \sim 2.5$–3.5), light can leave the semiconductor only under a small angle θ_{c} from the surface normal due to total reflection (cf. (9.11) and see right part of Fig. 9.2). Against air ($n_1 \approx 1$) the critical angle is

$$\theta_{\text{c}} = \sin^{-1}(1/n_{\text{s}}) . \tag{23.7}$$

The critical angle for total reflection is 16° for GaAs and 17° for GaP. Additionally, a portion of the photons that do not suffer total reflection is reflected back from the surface with the reflectance R given by (cf. (9.15))

---

[12] Note that the light extraction efficiency is also important for solar cells, cf. Sect. 22.4.3.

$$R = \left(\frac{n_s - 1}{n_s + 1}\right)^2 . \tag{23.8}$$

We note that the above formula is valid strictly for vertical incidence. For the GaAs/air interface, the surface reflectance (for normal incidence) is about 30 %. Thus, the light extraction efficiency for a LED is given by $(1-R)$ and the critical angle by

$$\chi_{ex} \cong \frac{4\,n_1\,n_s}{(n_1 + n_s)^2}\,(1 - \cos\theta_c) \approx \frac{4\,n_s}{(n_s + 1)^2}\,(1 - \cos\theta_c) . \tag{23.9}$$

The latter approximation is valid when the outer medium is air. For GaAs, the light extraction efficiency is $0.7 \times 4\,\% \approx 2.7\,\%$. Thus, for this simple geometry, only a small fraction of generated photons can leave the device and contribute to the LED emission.

23.3.4 Device Design

In the following subsections the strategies that have allowed significant improvement of the extraction efficiency (Fig. 23.5) and thus LED performance are briefly discussed. The record by 2014 for light extraction efficiency is 89 % [1642], however not for a mass-produced device.

Nonplanar Surfaces

With curved surfaces, the problem of total reflection can be (partially) circumvented (Fig. 23.6). Spherically polished chips are feasible, but, very expensive. The epoxy seal of the standard LED case (Fig. 23.7a) and its shape play a similar role, however, with a smaller index of refraction than the semiconductor, and are important for the beam shape.

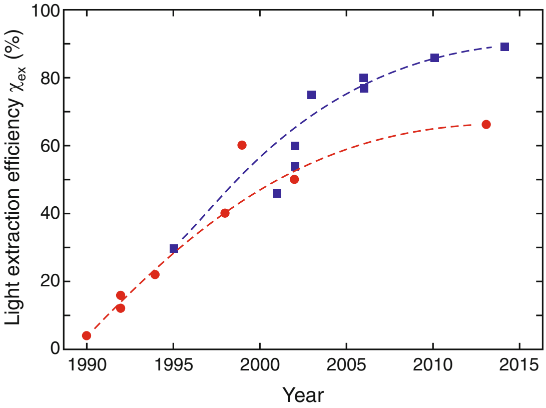

Fig. 23.5 Historic development of maximum light extraction efficiency for AlGaInP (*red circles*) and (In,Ga)N (*blue squares*) LEDs. *Dashed lines* are guides to the eyes. Adapted from [1637, 1643]

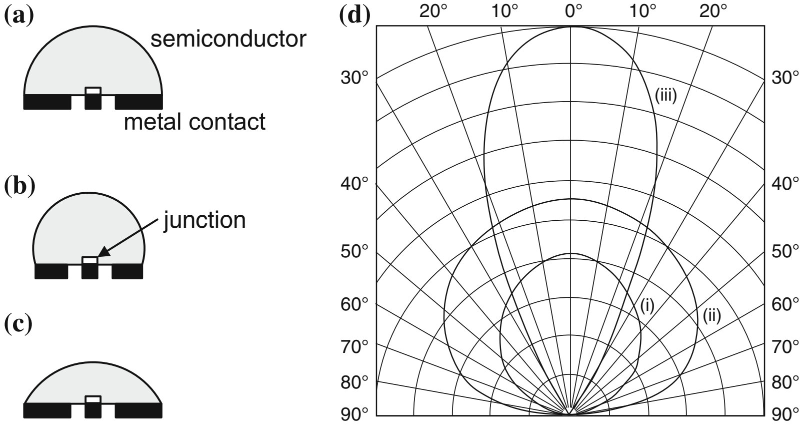

Fig. 23.6 Form of various LED casings with (**a**) hemispherical, (**b**) truncated sphere and (**c**) parabolic geometry. Adapted from [1644]. (**d**) Emission characteristics for rectangular (**i**), hemispheric (**ii**) and parabolic (**iii**) geometry. Adapted from [1645]

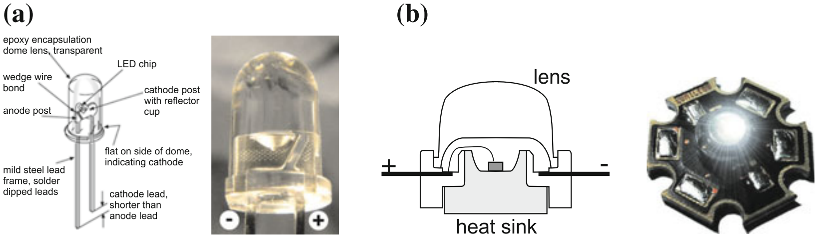

Fig. 23.7 (**a**) Standard LED casing (schematic drawing and macrophoto), (**b**) high-power mounting (schematic drawing and image of Luxeon® LED)

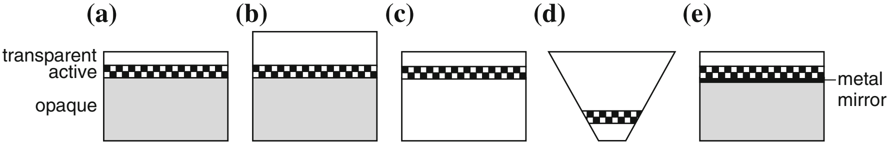

Fig. 23.8 (**a**) Standard LED layer sequence with opaque substrate (*grey*), active layer (*checkered*) and transparent top, (**b**) thick window design with thick top layer (50–70 µm). (**c**) Transparent substrate (by rebonding, see Fig. 23.9), (**d**) chip shaping (cf. also Fig. 23.11). (**e**) Thin-film LED with metal mirror (*black*) and rebonding (cf. also Fig. 23.12)

Thick-Window Chip Geometry

An increase in light extraction efficiency to about 10–12 % can be achieved if the top layer is fabricated with a much larger thickness (Fig. 23.8b) of 50–70 µm instead of a few µm. However, such approach is not scalable since larger device area would demand even larger thickness.

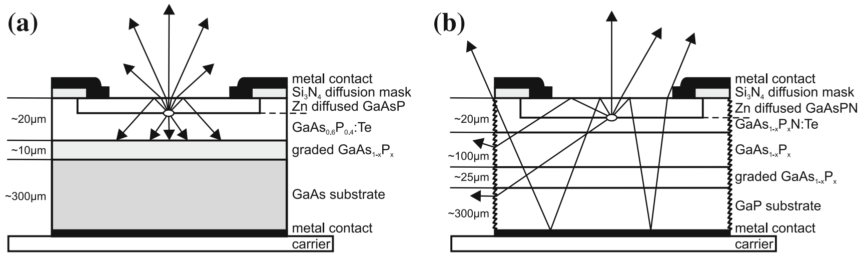

Fig. 23.9 Comparison of light paths in a GaAsP-based LED with (**a**) opaque (GaAs) and (**b**) transparent (GaP) substrate (side facets roughened). Adapted from [1646]

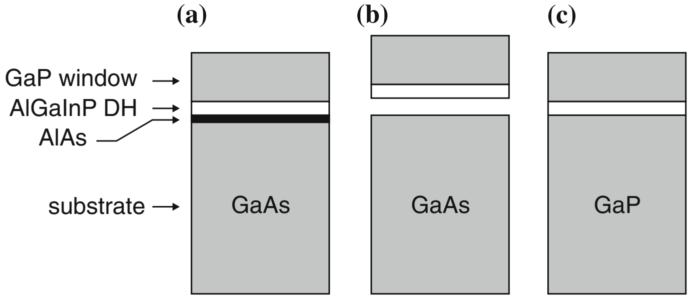

Fig. 23.10 Scheme of fabrication for red high brightness LED: (**a**) AlGaInP double heterostructure (DH) with GaP window on GaAs substrate (growth with MOCVD). (**b**) Lift-off using HF etch of sacrificial AlAs layer. (**c**) Wafer bonding on GaP (transparent for red light)

Transparent Substrate

Reflection of photons is not so detrimental if they are not lost later due to absorption in the substrate. In Fig. 23.8, the evolution of LED chip design is shown schematically. In Fig. 23.9, the light path is compared for opaque and transparent substrates. The latter provides higher light extraction efficiency due to the 'photon recycling' effect. Efficiencies of 20–25 % are possible. In Fig. 23.10, the technological steps are shown to fabricate a GaP LED with an AlGaInP active layer. The active layer is initially grown on GaAs due to lattice-match conditions.

Nonrectangular Chip Geometry

If the chip is made with an inverted structure and mounted on a mirror, a high light extraction efficiency (>50 %) can be achieved. Typical commercial designs are shown in Fig. 23.11.

The increase in quantum efficiency allows the devices to run on much higher output power. While initially LEDs delivered power only in the mW regime, now output power in the $\sim$1 W regime is possible (high brightness LEDs). The higher currents made a redesign of the LED mount towards better heat sinks necessary (Fig. 23.7b). While the standard case has a thermal resistance of 220 K/W

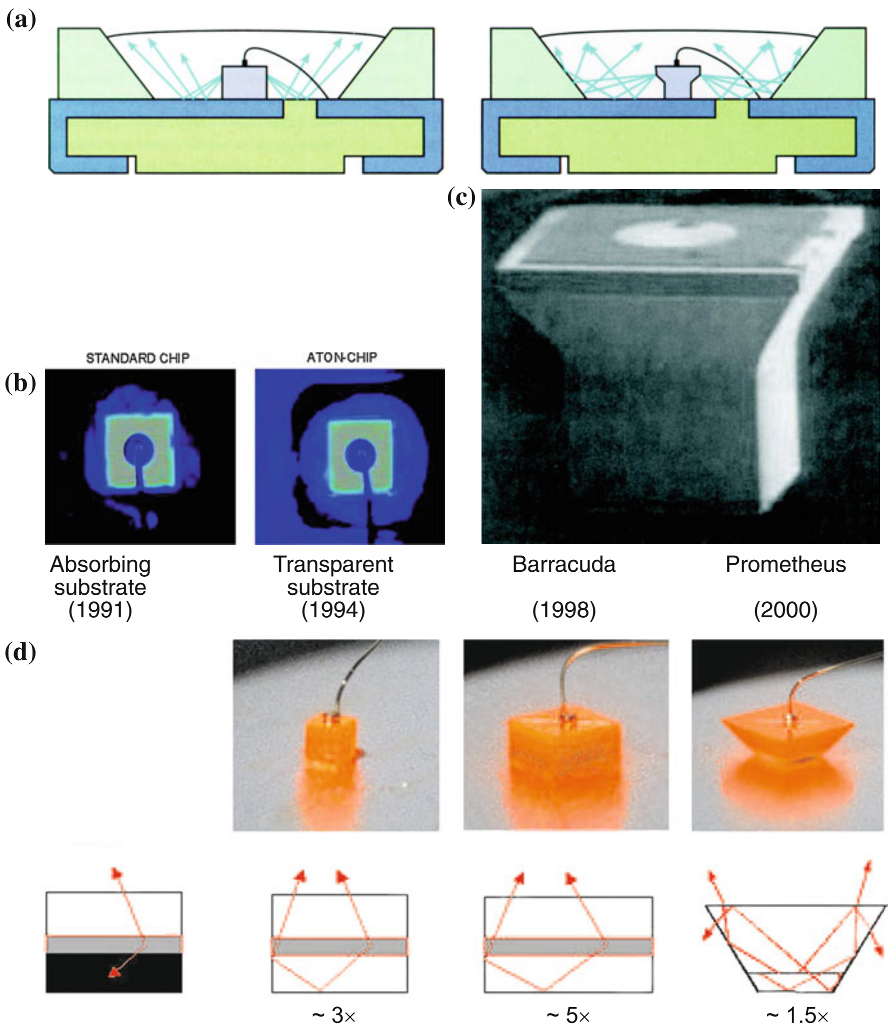

Fig. 23.11 Optimization of light exit by 3D design of the LED chip, (**a**) scheme, (**b**) emission pattern comparison and (**c**) SEM image of the ATON chip. Reprinted with permission from [1647]. (**d**) Development stages towards the truncated inverted pyramid (Prometheus) chip. From [1648]

(chip size $(0.25\,\mathrm{mm})^2$ for 0.05–0.1 W and 0.2–2 lm), the high-power case has 15 K/W (chip size $(0.5\,\mathrm{mm})^2$ for 0.5–2 W and 10–100 lm). An epoxy-free technique for encapsulation also enhances the color uniformity and maintains the brightness.

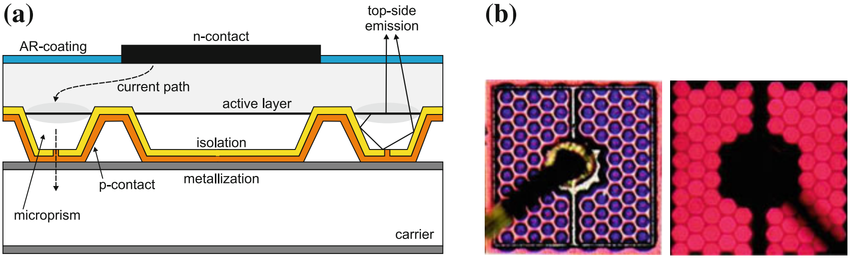

Fig. 23.12 (**a**) Scheme of thin-film flip-chip LED with microprisms. (**b**) image and luminescence image of thin film AlInGaP LED (chip length: 320 μm). Reprinted with permission from [1650]

Thin-Film LED

In the thin-film LED design [1649], as schematically shown in Fig. 23.12a, a metal mirror is evaporated on the LED layers. In a flip-chip design, subsequently the metal side is wafer bonded to another metallized substrate and the original substrate is removed. Additionally, the LED surface can be patterned (before bonding) into an (hexagonal) array of (hexagonal) microprism mesas with an insulating (e.g. silicon nitride) layer with openings in order to optimize the current path. The microprisms are optimized to allow efficient reflection of light towards the emitting surface. This technology is scalable to large areas without loss in efficiency.

In order to avoid bonding from the top which leads to partial shielding of the emitted radiation and is a mechanical process, contact schemes for flip-chip LEDs have been devised for contacting both the n- and the p-layer from the same side [1651]. In Fig. 23.13 a schematic cross-section and an emission image are shown. Here, the n-contact runs through a via hole with insulated side walls. In the emission image the array of via holes can be seen.

Bulk Flip-Chip

In the GaN material system a LED based on a triangular chip with 400 μm side length using a bulk substrate with 150 μm thickness has been presented that exhibits the so

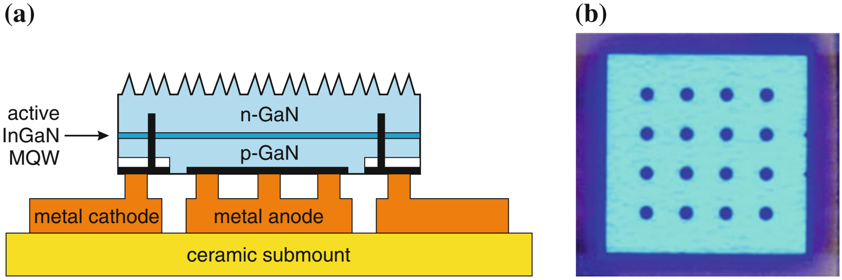

Fig. 23.13 (**a**) Scheme of thin-film flip-chip LED with rough surface and contacts from one side. (**b**) Emission image of 1 × 1 cm^2 chip. Adapted from [1651]

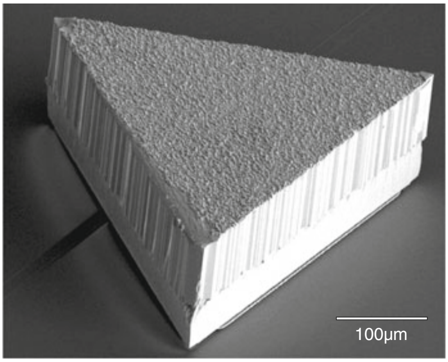

Fig. 23.14 Triangular GaN LED chip with high extraction efficiency. Both the p- and n-contact are on the bottom. Adapted from [1642]

far highest extraction efficiency of almost 90 % (Fig. 23.14) [1642, 1652]. The top and all side facets are rough.

23.3.4.1 Cascaded LEDs

Similar to the use of tunneling junctions in multi-junction solar cells (Fig. 22.64), the monolithic serial connection of several LED layers has been proposed [1653] (Fig. 23.15). For a given output power P at forward voltage V_F and current density j of a single junction LED, ideally a LED with N identical stacks and $N-1$ tunneling junctions provides the same output power P at the N-fold forward voltage, as reported for $N = 2, 3$ in [1654], and the current density j/N. Since the internal quantum efficiency of LEDs decreases with increasing current density (*droop*), such stacked LED design holds promise for increased wall-plug efficiency if the series resistance of the tunneling junctions is small. The quantum efficiency of such device is then larger than N times the efficiency of the single stack LED and thus way larger than 100% (similar to quantum cascade lasers, Sect. 23.4.16).

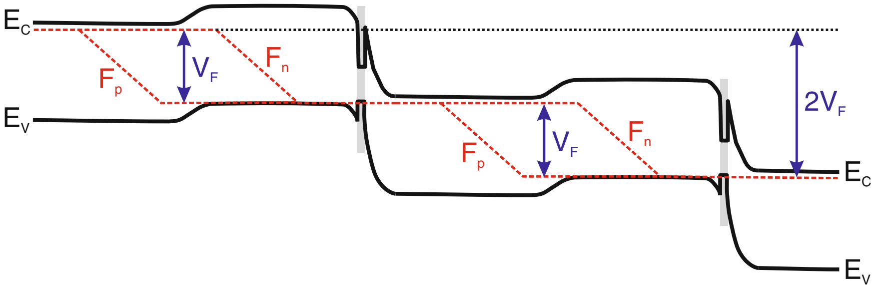

Fig. 23.15 Schematic band structure of cascaded LED. The *grey area* denotes an additional heterostructure for reduction of the series resistance of the tunnel junctions. Adapted from [1653]

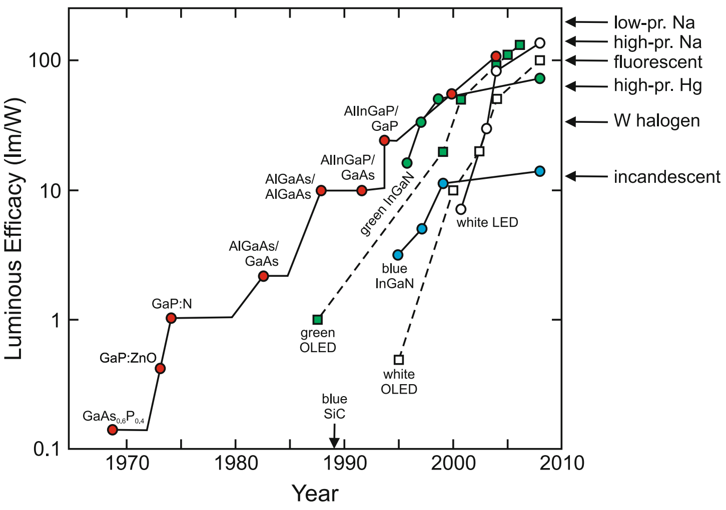

Fig. 23.16 Historic development of the luminous efficacy of semiconductor LEDs and OLEDs. Based on [1655] with the addition of data on OLEDs and recent data on LEDs. The arrows on the right indicate efficacy of various other light sources

Fig. 23.17 Historic development of the flux (in lumen) and cost (in \$/lm) for semiconductor LEDs. Data from [1648]

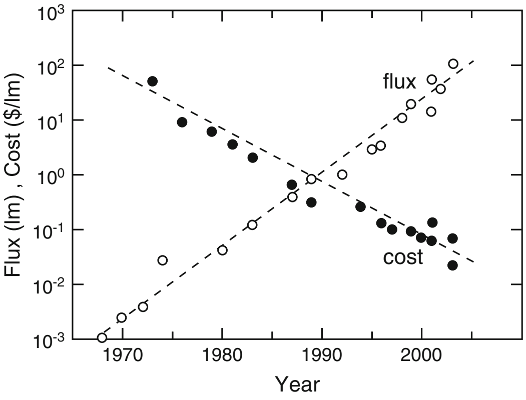

Historic Development

In Fig. 23.16, the historic development of the LED luminous efficacy (luminous flux per electrical input power) is shown for various material systems. While the luminosity has increased by a factor of 20 per decade in the last 40 years, the price has decreased by a factor of ten per decade (Fig. 23.17). Currently, there is a need for the development of efficient LEDs in the green spectral range since their luminosity is small compared to devices for the blue and red spectral regions (Fig. 23.18).

Fig. 23.18 Luminous performance of various LED materials in comparison with other light sources. Adapted from [1655]

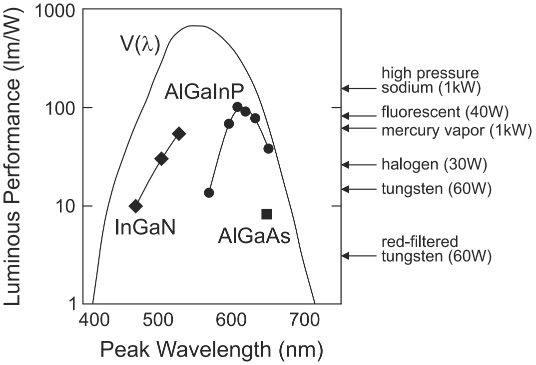

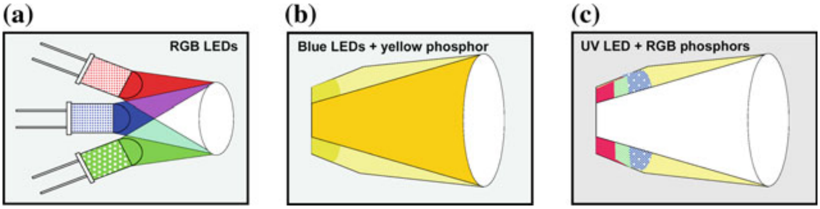

Fig. 23.19 Different strategies to generate white light with LEDs. (**a**) Additive mixing of R, G, and B LEDs, (**b**) blue LED and yellow phosphor, (**c**) UV LED (invisible) and R, G, and B phosphors. From [1648]

23.3.5 White LEDs

There are different possibilities to generate white light with an LED as shown schematically in Fig. 23.19. The highest color gamut and a tunable white point can be achieved by combining a red, a green and a blue LED (Fig. 23.19a). Using a blue LED and a yellow phosphor (Figs. 23.19b and 23.20a, b), a white spectrum can be achieved that is, however, not very close to a blackbody spectrum (Fig. 23.20c). A better color rendering can be obtained with the combination of two phosphors [1656]. With an UV LED that is itself invisible (and must be shielded so no UV radiation leaves the LED), phosphors with various colors can be pumped (Fig. 23.19c). The mix of phosphors determines the white point.

Using a blue-emitting LED based on (In,Ga)N material, phosphors (similar to those used in fluorescence lamps) can be pumped. Blue light is converted into green, yellow or red light such that the resulting total spectrum appears white to the human eye. Also, a broad range of other colors can be designed (color on demand), e.g. pink or particular corporate colors.

The color of a white LED depends on the operation conditions. In Fig. 23.21a the intensity versus dc driving current characteristic of a white LED is shown. In Fig. 23.21b the chromaticity coordinates are shown for various dc currents. A change of wavelength with forward voltage occurs for the blue-emitting (In,Ga)N material

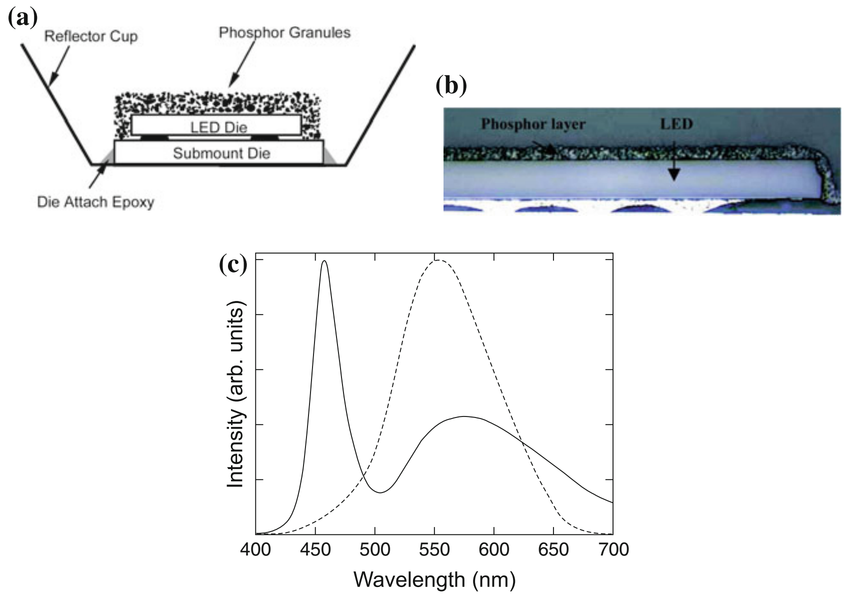

Fig. 23.20 (**a**) Scheme and (**b**) image of color conversion Luxeon® LED. From [1648]. (**c**) Spectrum (*solid line*) of white LED with blue LED pumping a yellow phosphor together with eye-sensitivity curve $V(\lambda)$ (*dashed line*). Adapted from [1650]

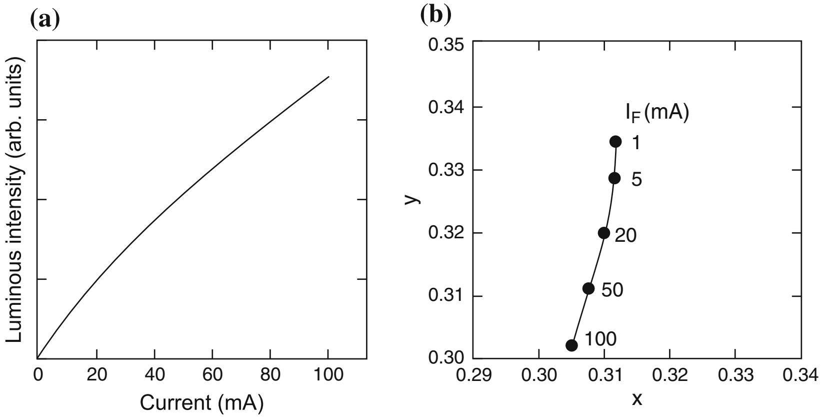

Fig. 23.21 (**a**) Luminous intensity of white LED (NSCW215) versus dc forward current. (**b**) CIE chromaticity coordinates for various dc driving conditions as labeled. Data taken from [1657]

due to filling of low-energy states (Fig. 23.22). In order to avoid this effect, the LED is driven with pulses of a fixed current amplitude and a repetition frequency that is high enough to provide a flicker-free image to the human eye, e.g. 100 Hz. The

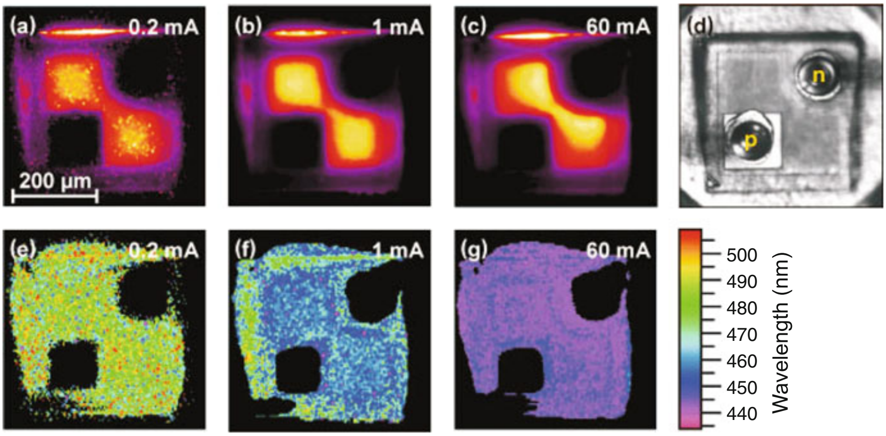

Fig. 23.22 (**a**–**c**) Electroluminescence intensity map of (In,Ga)N LED at different currents as labeled. (**d**) Optical image of the LED chip (*top view*). (**e**–**g**) Wavelength images (wavelength of spectral emission maximum) for different currents. Adapted from [1658]

intensity of the LED is modulated via the pulse width, i.e. between 0–10 ms in this case (PWM, pulsewidth modulation).

The direct light from white LEDs is visually appealing and cannot be distinguished from a blackbody source of matching temperature. But since the spectral power distribution of white LEDs is different from natural light, objects illuminated by such light source can appear in 'wrong' colors. For the spectrum of Fig. 23.20c, in particular green is reproduced poorly. A quantitative measure for the ability of a light source to reproduce the colors of an illuminated object faithfully compared with a natural (blackbody) light source is the *color rendering index* (CRI).

A major advantage of LEDs for display and lighting applications is their long lifetime compared to halogen (about 2000 h), xenon (10,000 h) or fluorescent (6000–10,000 h) lights. Philips Lumileds projects (for white LUXEON® K2 LEDs)

Fig. 23.23 Lifetime for 70 % lumen as a function of solder temperature T_s (for white Diamond Dragon® LED) for various driving currents (0.3, 0.7, 1.4 and 2.0 A, *solid lines* from right to left). The *dashed line* is for low driving current and $T_s = T_j$. Adapted from [1662]

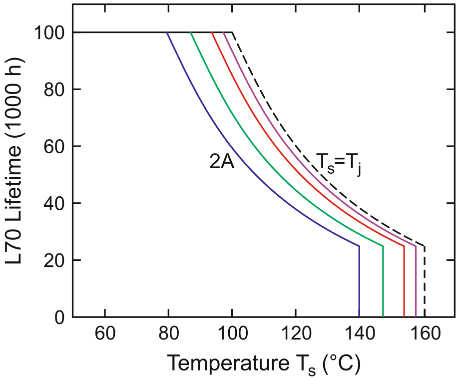

70 % lumen maintenance at given current (1 A) at 50,000 h for junction temperature $T_{\mathrm{j}} \leq 120°$ [1659]. Similar values are given by OSRAM [1662] for white high power LEDs (Fig. 23.23). A current problem is the decrease of efficiency with increasing current density termed *droop*, probably due to Auger recombination [1660, 1661].

23.3.6 Quantum Dot LEDs

Quantum dots are an interesting active medium for LEDs due to their spectroscopic properties (Sect. 14.3.4).

Ultranarrow Spectral Emission

A LED based on a single QD exhibits a rather unique spectrum consisting of a single spectral line, at least at low temperatures [1663], due to exciton recombination as shown in Fig. 23.24. Such device can deliver single photons on demand and be a photon source for quantum cryptographic communication. At higher current also biexciton recombination appears. In [1664, 1665] the triggered emission of photon pairs from cascade-like XX and X recombination in a single dot and their polarization entanglement is reported. Entanglement is related to degenerate X and XX emission energy [1666] (cmp. Fig. 14.33).

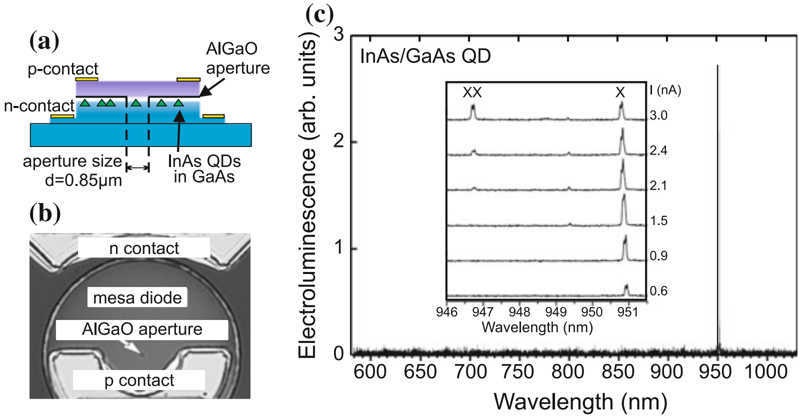

Fig. 23.24 (**a**) Schematic cross-section of QD LED. Current is fed to a single QD via an oxide aperture. (**b**) Plan-view SEM image of QD LED. **c** Electroluminescence (EL) spectrum ($T = 10\,\mathrm{K}$, $U = 1.65\,\mathrm{V}$, $I = 0.87\,\mathrm{nA}$) of single InGaAs/GaAs QD LED (diameter of oxide aperture $0.85\,\mu\mathrm{m}$, thickness 60 nm). The single line is due to (neutral) exciton recombination. The *inset* shows dependence of EL spectrum on injection current; at higher currents a second peak due to biexciton recombination (XX→X) appears. Adapted from [1667]

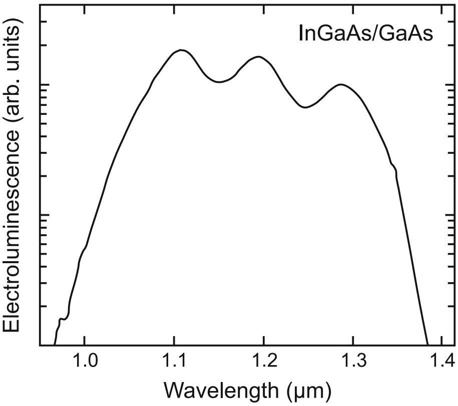

Fig. 23.25 Electroluminescence spectrum of a quantum dot LED designed for broad spectral range (at 5 kA/cm^2). Adapted from [1669]

Ultrabroad Spectral Emission

An LED based on the emission from a quantum dot ensemble exhibits a fairly broad spectrum because of inhomogeneous broadening due to size fluctuations of the quantum dots (cmp. Fig. 14.36). Additionally several ensembles of QDs with different mean emission wavelength can be incorporated in a device, e.g. in stacked layers [1668]. This way ultrabroad electroluminescence spectra can be realized (Fig. 23.25). Also emission on the ground and excited state can be used for broad spectral emission.

23.3.7 Organic LEDs

An organic light emitting diode (OLED) is made from organic semiconductors. The pioneering work was made by Tang and Van Slyke [1503, 1670]. Typical layer sequences are depicted in Fig. 21.60. The light emission occurs through the anode (and the transparent ITO layer) while the metal cathode is opaque. Two major configurations are possible, emission through the transparent substrate (glass) or top emission (Fig. 23.26).

The optimization of materials for the various functional layers is ongoing. The emission layer (EML) is optimized for efficient radiative recombination for the design wavelength or wavelength range. The highest efficacy of over 100 lm/W (Fig. 23.16) is achieved using phosphorescent materials (Sect. 17.6). The contacts are optimized for high carrier injection efficiency and the transport layers are optimized for high conductivity.

End of 2007 a transparent white OLED panel was introduced [1671] (Fig. 23.27a). Its transparency is 55 % and shall be improved in the future. A crucial point is

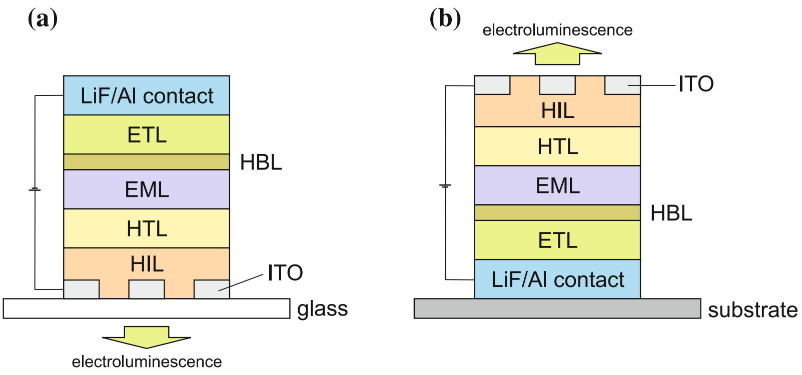

Fig. 23.26 Typical OLED design for (**a**) bottom and (**b**) top emission

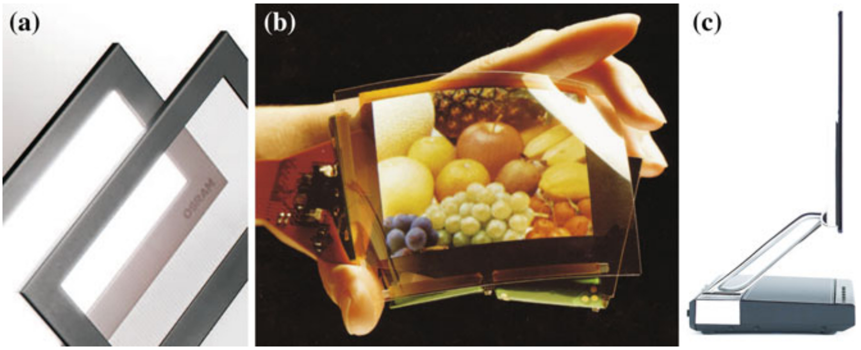

Fig. 23.27 (**a**) Transparent OLED panel. From [1671]. (**b**) Flexible OLED display. From [1672]. (**c**) 3 mm thin, 11 inch diagonal OLED TV. From [1673]

the protection of the organic films against moisture and air. The encapsulation by glass is very good. Flexible OLED panels with polymer substrate and encapsulation have been demonstrated (Fig. 23.27b). OLED technology is currently used for small displays in digital cameras and cellular phones. It enables very thin TV panels, only a few mm thick (Fig. 23.27c) entering the mass market in 2010. An increase of the lifetime from 30,000 to beyond 50,000 h is expected.

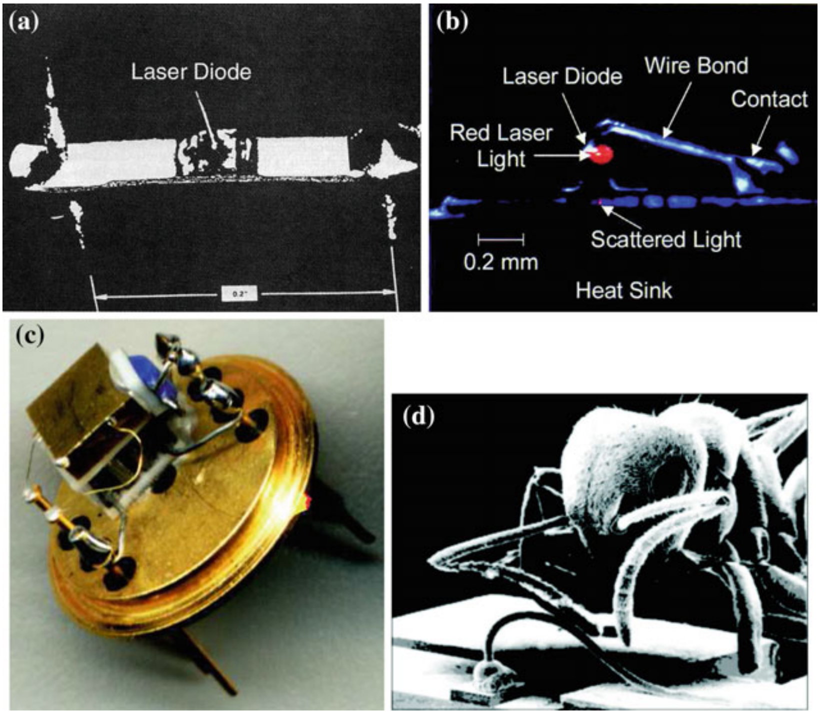

Fig. 23.28 Images of the first semiconductor lasers, 1962: (**a**) GaAs laser, Lincoln Laboratories and (**b**) GaInP laser, N. Holonyak and S.F. Bevacqua, Urbana Champaign. (**c**) Laser (at the end of gold bond wire) mounted on Peltier heat sink and a TO chip, Universität Leipzig. (**d**) Size comparison of an ant with a laser chip (underneath the bond wire)

23.4 Lasers

23.4.1 Introduction

Semiconductor lasers[13] [1674, 1675] contain a zone (mostly called the *active layer*) that has gain if sufficiently pumped and that overlaps with an optical wave. The wave bounces back and forth in an optical cavity that leads to optical feedback. The part of the wave that exits the semiconductor forms the laser beam. Some of the first semiconductor lasers and a mounting design are shown in Fig. 23.28.

---

[13] The term 'laser' is an acronym for 'light amplification by stimulated emission of radiation'. The amplification relies on stimulated emission, theoretically predicted by Einstein in 1917. The laser concept was first explored in the microwave wavelength region (1954, MASER using ammonia, Ch.H. Townes, Nobel prize 1964). The first optical laser (1958, US patent No. 2,929,922 awarded 1960, A.L. Schawlow, Ch.H. Townes) was the ruby laser developed in 1960 by Th. Maiman. A device is a laser when it emits stimulated light. This light must neither be monochromatic nor be emitted in a narrow, directed beam.

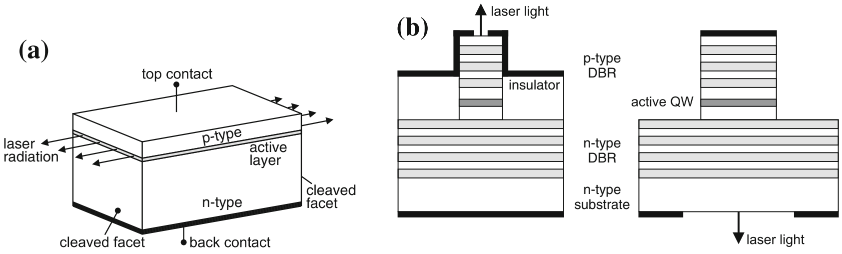

Fig. 23.29 (**a**) Schematic drawing of edge-emitting semiconductor laser. (**b**) Schematic drawings of vertical-cavity surface-emitting lasers with top emission (*left*) and emission through the substrate (*right*). *Black areas* are metal contacts

Generally, two main geometrical laser types, *edge* emitters (Fig. 23.29a) and *surface* emitters (Fig. 23.29b), are distinguished. The emission of the edge emitter exits through cleaved {110} side facets[14] (≈30 % reflectance), of which an opposite pair acts as a Fabry–Perot optical cavity. The surface emission is directed along (001), since this is the (standard) growth direction of the heterostructure sequence making up the laser. The mirrors in a vertical-cavity surface-emitting laser (VCSEL) are made from dielectric Bragg mirrors (cf. Sect. 19.1.4) with typically $R > 99.6\,\%$. Using antireflection coating on one facet, semiconductor lasers can be set up with an external cavity.[15] If both facets are antireflection coated, feedback is missing and the chip can be used as an optical amplifier (cf. Sect. 23.5).

Most lasers are pn-diodes and are then called laser diodes. They rely on the gain of interband transitions and the emission wavelength is determined and (more or less) given by the band gap of the semiconductor. The cascade laser [1676] (Sect. 23.4.16) is a unipolar structure with a superlattice as active layer. Here, the intersubband transitions (mostly in the conduction band but also in the valence band) carry the gain. The emission wavelength depends on the subband separation and lies typically in the far- and mid-infrared. Extensions to the THz regime and also to shorter wavelengths are possible. A third type of laser is the ‘hot-hole’ laser (Sect. 23.4.17), typically fabricated with p-doped Ge, which can be viewed as unipolar and functions only in a magnetic field; its emission is in the THz regime.

23.4.2 Applications

In Fig. 23.30, the revenue in the worldwide diode laser market is shown. The drop after 2000 is due to the burst of the ‘internet bubble’. Nondiode laser (gas, ruby,

---

[14] Or etched facets in possibly any direction.

[15] Such external cavities can be used for manipulation of the laser properties such as wavelength tuning.

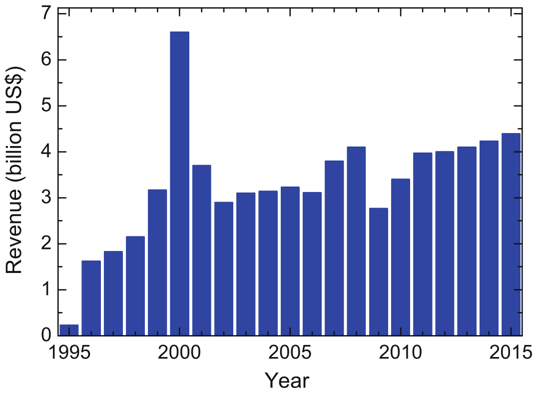

Fig. 23.30 Revenue in worldwide diode laser market. Based on numbers from [1677], data or 2015 estimated

excimer, …) revenue is currently stable at around 2 billion US$, thus semiconductor lasers account for the largest share of all laser types sold.

The following applications rely on semiconductor lasers:

- optical communication, mostly optical fiber based (senders), typically at 10 GBit/s, in special situations also 40 GBit/s data rate.
- optical information storage and retrieval (CD, DVD, BD[16]) with as short of a wavelength as possible, as shown in Fig. 23.31, currently 405 nm.
- pumping of solid-state lasers, typically 910 or 940 nm for pumping Nd:YAG.
- portable projectors, laser TV, entertainment.
- laser pointers, see Fig. 23.32. A red laser pointer simply uses the collimated red emission of a GaAs-based diode. In a green laser pointer, an infrared diode pumps a Nd:YAG or Nd:YVO_4 crystal. The emitted beam is then frequency doubled, typically with a $KTiOPO_4$ (KTP) crystal.
- medical instruments with a variety of wavelengths in ophthalmology, dermatology, cosmetics (hair removal, tattoo removal).
- various other uses, such as remote control, position detection, distance measurement, printing, scientific instrumentation.

The market for photonic devices is much more dynamic than the electronics market. An example is the rapid change of dominating laser applications. For diode lasers, the two most prominent applications are telecommunication (77 % market share in 2000, 25 % in 2003, 45 % in 2008) and optical data storage (17 % market share in 2000, 60 % in 2003, 44 % in 2008).

---

[16] 16 million 405 nm laser diodes were shipped in 2006–2008. 85 % of those are built into SONY's PS3, the rest into HD-DVD and other Blu-ray™disc (BD) players.

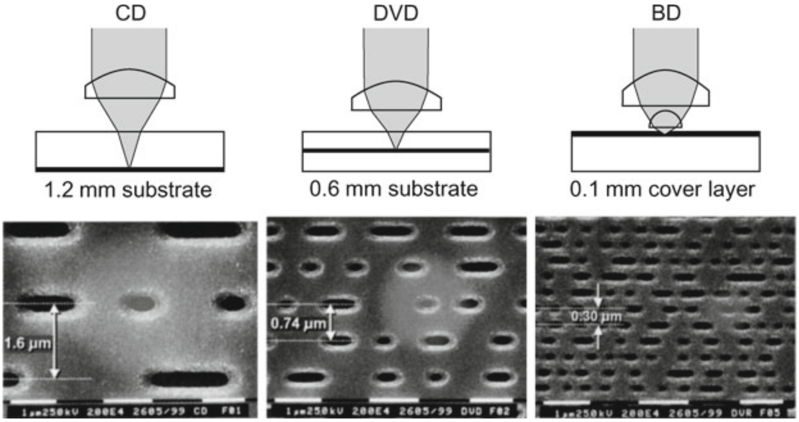

Fig. 23.31 Evolution of optical data storage technology, ‘CD’: compact disk (laser: 780 nm, pitch: 1.6 µm, capacity: 0.7 GB), ‘DVD’: digital versatile disk (laser: 635–650 nm, pitch: 0.74 µm, capacity: 4.7 GB for one layer), ‘BD’: ‘Blu-ray’ disk (laser: 405 nm, pitch: 0.32 µm, capacity: 27 GB for one layer)

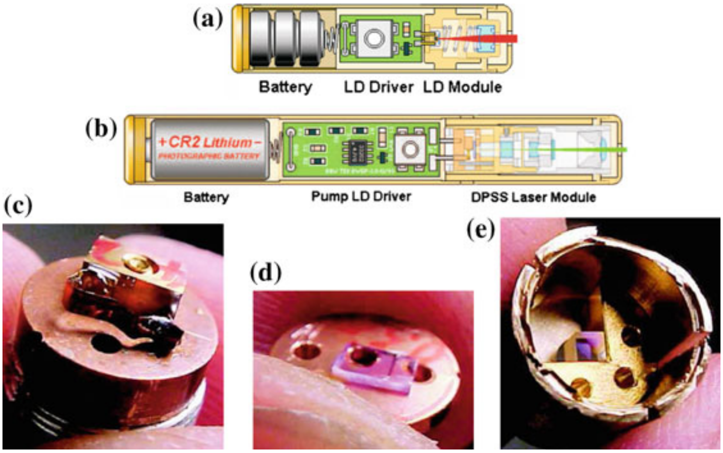

Fig. 23.32 (**a**) Scheme of red laser pointer, (**b**) scheme of green laser pointer. Parts of a green laser pointer: (**c**) pump laser diode, (**d**) YVO_4 crystal, (**e**) KTP doubler

23.4.3 Gain

Due to current injection,[17] a nonequilibrium carrier distribution is created. After fast thermalization processes (phonon scattering), it can mostly described by quasi-Fermi

---

[17] Or due to optical pumping. If electrical contacts are not available, the laser action can be invoked by supplying a high-intensity light beam, possibly in a stripe-like shape. For optically pumped semiconductor lasers see Sect. 23.4.15.

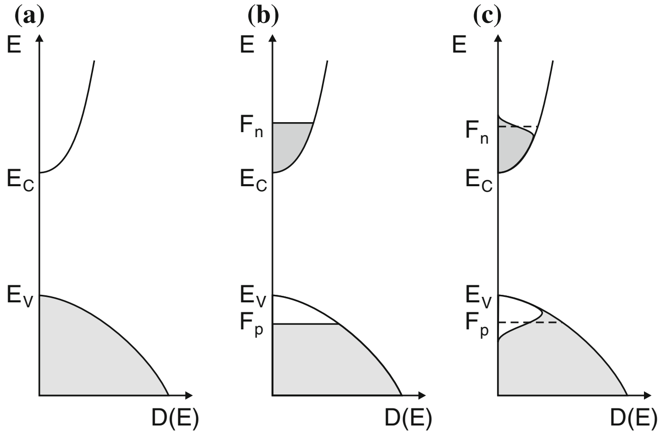

Fig. 23.33 Population (**a**) in thermodynamic equilibrium $T = 0\,\mathrm{K}$, (**b**) under inversion for $T = 0\,\mathrm{K}$, (**c**) under inversion for $T > 0\,\mathrm{K}$. *Shaded areas* are populated with electrons

levels. Sufficiently strong pumping leads to inversion, i.e. conduction-band states are more strongly populated with electrons than valence-band states (Fig. 23.33). In this case, the stimulated emission rate is stronger than the absorption rate (cf. Sect. 10.2.6). The thermodynamic laser condition (cf. (10.23)) requires the difference of the quasi-Fermi levels to be larger than the band gap.

$$F_\mathrm{n} - F_\mathrm{p} > E_\mathrm{g} \tag{23.10}$$

The gain is defined as the (frequency-dependent) coefficient $g(\hbar\omega)$ that describes the light intensity along a path L according to

$$I(L) = I(0)\, \exp\left(g\, L\right) . \tag{23.11}$$

The gain spectrum as a function of the photon energy $\hbar\omega$ is given for non-k-conserving recombination by (cf. (10.5) and (10.6))

$$g(\hbar\omega) = \int_0^{\hbar\omega - E_\mathrm{g}} D_\mathrm{e}(E) D_\mathrm{h}(E') \left[f_\mathrm{e}(E) f_\mathrm{h}(E') - (1 - f_\mathrm{e}(E))(1 - f_\mathrm{h}(E')) \right] \mathrm{d}E , \tag{23.12}$$

with $E' = \hbar\omega - E_\mathrm{g} - E$. The gain is positive for those photon energies for which light is amplified and negative for those that are absorbed. In Fig. 23.34a, the electron and hole concentrations are shown for GaAs as a function of the quasi-Fermi energies. In Fig. 23.34b, the difference of the quasi-Fermi energies is shown as a function of the carrier density (for neutrality $n = p$). The gain spectrum is shown in Fig. 23.34c

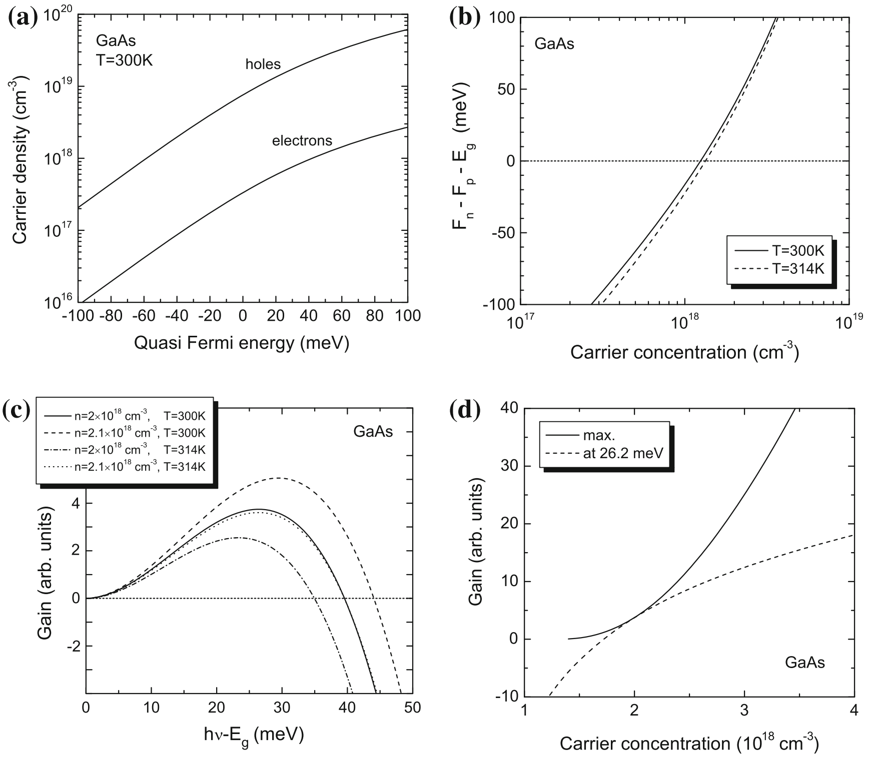

Fig. 23.34 Gain in the two-band model for GaAs. (**a**) Electron and hole concentrations at $T = 300\,\mathrm{K}$ as a function of the quasi-Fermi energies counted relative to the band edges, i.e. $F_\mathrm{n} - E_\mathrm{C}$ and $E_\mathrm{V} - F_\mathrm{p}$. (**b**) Difference of quasi-Fermi levels as a function of carrier concentration ($n = p$) for GaAs at two different temperatures. (**c**) Gain spectra according to (23.12) for $n = 2 \times 10^{18}$ and $T = 300\,\mathrm{K}$ (*solid line*), increased carrier density $n = 2.1 \times 10^{18}$ and $T = 300\,\mathrm{K}$ (*dashed line*), higher temperature $n = 2 \times 10^{18}$ and $T = 314\,\mathrm{K}$ (*dash-dotted line*) and same difference of the quasi-Fermi levels as for the *solid line*, $n = 2.1 \times 10^{18}$ and $T = 314\,\mathrm{K}$ (*dotted line*). (**d**) Maximum gain (*solid line*) and gain at a particular energy (*dashed line*, for photon energy $E_\mathrm{g} + 26.2\,\mathrm{meV}$ for which the gain is maximal for $n = 2 \times 10^{18}$ and $T = 300\,\mathrm{K}$, see *solid line* in part (**c**))

for a simple two-band model.[18] For a more elaborate discussion of such matters we refer to [1678]. In the case of inversion, the gain is positive for energies between E_g and $F_\mathrm{n} - F_\mathrm{p}$. At $\hbar\omega = F_\mathrm{n} - F_\mathrm{p}$, the gain is zero (transparency) and for larger energies negative (positive absorption coefficient). The agreement of experimental gain spectra of quantum wells with theoretical considerations, including carrier collision effects at the level of quantum kinetic theory in the Markovian limit, is very good (Fig. 23.35a) [1679].

---

[18] One electron and one hole band are considered; the heavy and light hole bands are taken into account via the mass according to (6.69).

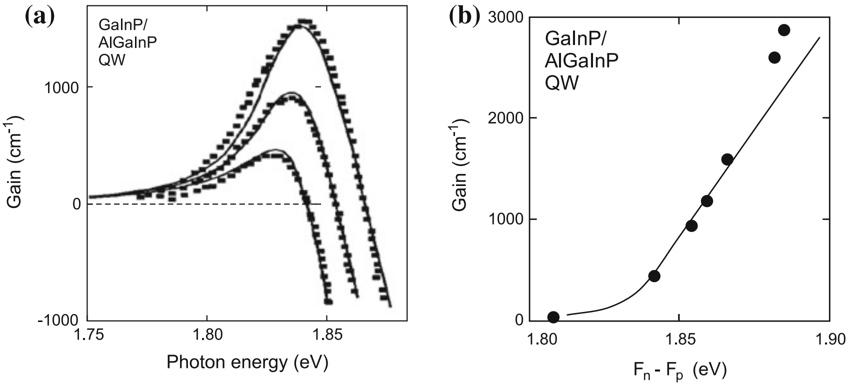

Fig. 23.35 (**a**) Gain spectra of a 6.8 nm thick $Ga_{0.41}In_{0.59}P$/ $(Al_{0.5}Ga_{0.5})_{0.51}In_{0.49}P$ quantum well, experimental data (*symbols*) and theory (*lines*) for three different sheet carrier densities $n_{2D} = 2.2$, 2.7, and $3.2 \times 10^{12}\,cm^{-2}$. (**b**) Maximum gain as a function of the separation of the quasi-Fermi levels, experimental data (*symbols*) and theory (*lines*). Adapted from [1679]

For a given fixed energy, the gain increases with increasing pumping and increasing carrier density n (Fig. 23.34d). For very small density, it is given as $g(n \to 0) = -\alpha$. The gain rises around transparency approximately linearly with the pumping intensity. At transparency carrier density n_{tr}, the gain is zero. Therefore, the relation $g(n)$ can be approximated as (linear gain model)

$$g(n) \cong \hat{\alpha}\,\frac{n - n_{tr}}{n_{tr}}. \tag{23.13}$$

For large carrier density, the gain saturates (at a value similar to α). The onset of positive gain is related to the separation of the quasi-Fermi levels being larger than the band gap (23.10), Fig. 23.35b. The gain in quantum dot lasers [1680] has been discussed in [1681].

23.4.4 Optical Mode

The light wave that is amplified must be guided in the laser. An optical cavity is needed to provide optical feedback such that the photons travel several times through the gain medium and contribute to amplification. We explain the light-wave management for the edge emitter first:

Vertical Mode Guiding

In the course of the historical development of the semiconductor laser, the most significant improvements (reduction of lasing threshold current) have been achieved through the improvement of the overlap of the optical wave with the gain medium, as

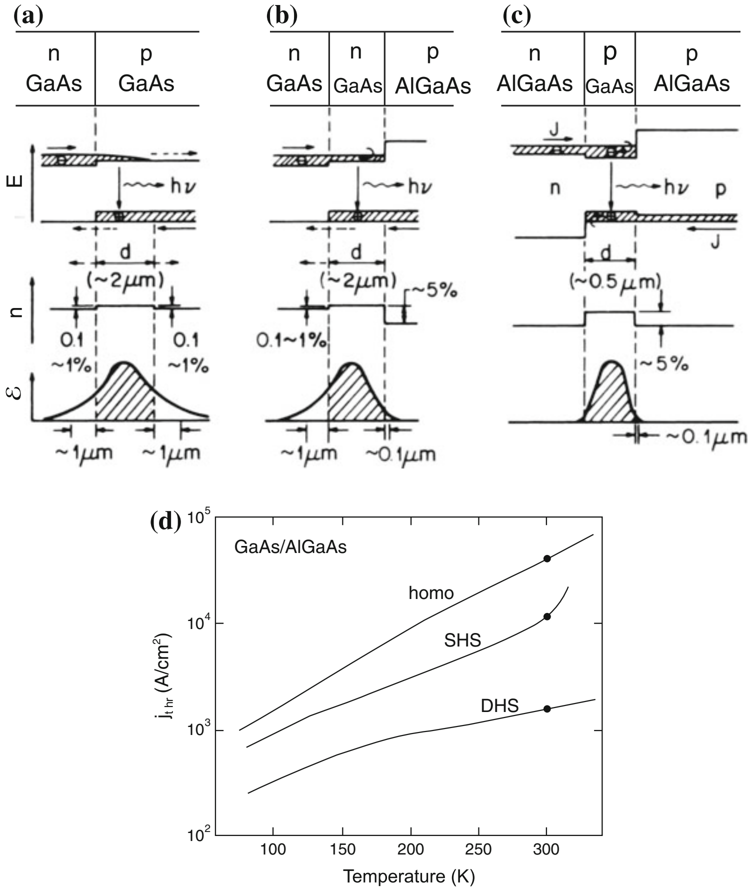

Fig. 23.36 Laser with (**a**) homojunction, (**b**) single heterostructure (SHS), (**c**) double heterostructure ('DHS'), (**d**) reduction of threshold current with design progress ('SHS': $d = 2\,\mu$m, 'DHS': $d = 0.5\,\mu$m). Adapted from [1682]

shown in Fig. 23.36. From homojunctions over the single heterojunction, eventually the double heterostructure (DHS) design could reduce the laser threshold current density to the 1 kA/cm^2 level.

The band diagram of a double heterostructure is shown in Fig. 23.37 for zero and forward bias. In the DHS, the optical mode is guided by total reflection within the low band gap center layer, which has a larger index of refraction than the outer, large band gap layer.[19] When the layer thickness is in the range of λ/n_{r}, the form of the optical mode must be determined from the (one-dimensional) wave equation (Helmholtz equation) for the electrical field E_{z}

---

[19] A smaller band gap coincides for many cases with a larger index of refraction.

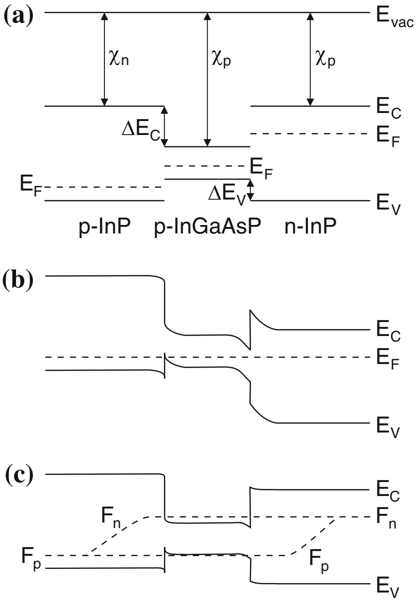

Fig. 23.37 Schematic band diagram of a pn double heterostructure (DHS) diode (InP/InGaAsP/InP) (**a**) before contact of the materials, (**b**) in thermodynamic equilibrium (zero bias, *dashed line* is Fermi level E_F = const.), (**c**) with forward bias close to flat-band conditions, *dashed lines* are quasi-Fermi levels

$$\frac{\partial^2 E_z}{\partial z^2} + \omega^2 \, \mu \, \epsilon(z) \, E_z = 0. \tag{23.14}$$

In Fig. 23.38a, the shape of the optical mode for GaAs/$Al_{0.3}Ga_{0.7}As$ DHS with different GaAs thickness is shown.

The optical confinement factor Γ is the part of the wave that has geometrical overlap with the gain medium, i.e. is subject to amplification. It is shown for GaAs/$Al_xGa_{1-x}As$ DHS with different GaAs thickness and different Al concentration in Fig. 23.38b. The modal gain g_{mod} that is responsible for light amplification in the cavity consists of the material gain g_{mat} due to inversion and the optical confinement factor.

$$g_{\mathrm{mod}} = \Gamma \, g_{\mathrm{mat}}. \tag{23.15}$$

In order to allow simultaneous optimization of the light mode and the carrier confinement, the separate confinement heterostructure (SCH) has been designed. Here, a single or multiple quantum well of a third material with even smaller band gap is the active medium (Fig. 23.39a, b, d). A single quantum well has an optical confinement factor of a few per cent only. It offers, however, efficient carrier capture and efficient radiative recombination. An increase in the carrier capture efficiency can be achieved using a graded index in the barrier (GRINSCH, Fig. 23.39c).

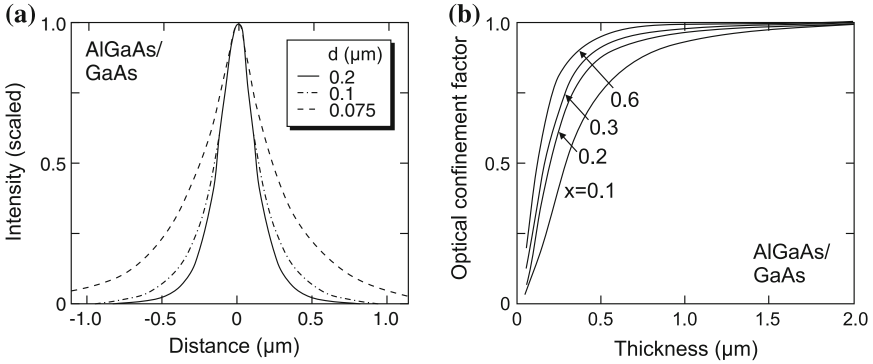

Fig. 23.38 (**a**) Optical mode (relative intensity) for various values of the thickness d of the active layer as labeled of a GaAs/Al$_{0.3}$Ga$_{0.7}$As DHS laser, (**b**) Optical confinement factor Γ as a function of the thickness of the active layer and the Al concentration x of the barrier as labeled in a GaAs/Al$_x$Ga$_{1-x}$As DHS laser. Adapted from [1674]

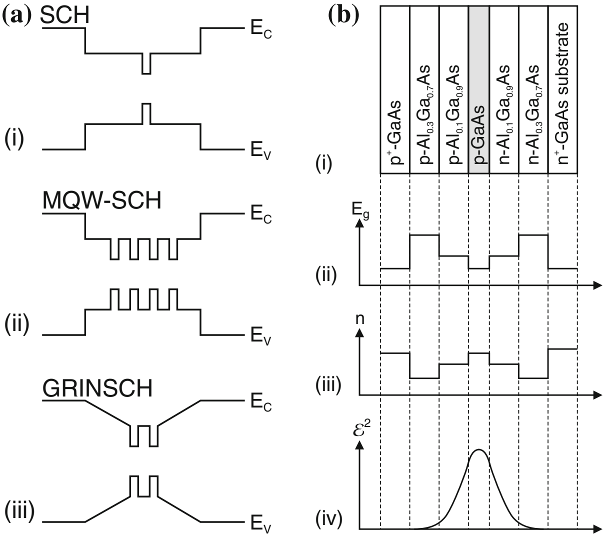

Fig. 23.39 (**a**) Various geometries of the active layer of a DHS laser with quantum wells as active medium, (**i**) single QW (separate confinement heterostructure, SCH), (**ii**) multiple QW SCH, and (**c**) GRINSCH (graded-index SCH) structure. (**b**) Layer sequence for a separate confinement heterostructure laser

The thin wave-guiding layer leads to large divergence of the laser beam along the vertical direction, typically about 90°. The strong confinement of light also limits the maximum achievable output power due to catastrophic optical damage (COD). Several ideas have been realized to overcome this problem and achieve much smaller divergence of about 18°. The waveguide can be designed to be very thick (large optical

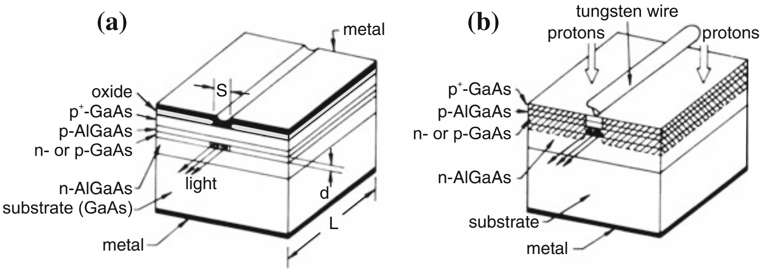

Fig. 23.40 Scheme of gain-guided lasers with stripe contact: (**a**) oxide stripe, (**b**) proton implanted with shadow mask from tungsten wire (∼10 μm). Adapted from [1683]

cavity, LOC) that leads to an increase of threshold. Other schemes are insertion of a low-index layer into the confinement layer, insertion of a high-index layer into the cladding layer or the use of high-index quarter-wavelength reflecting layers [1684].

Lateral Mode Guiding

Lateral waveguiding can be achieved with gain guiding and index guiding (or a mixture of the two). In the gain-guiding scheme (Fig. 23.40), the current path that is defined by the stripe contact and the current spreading underneath it, defines the gain region and therefore the volume of amplification that guides the optical wave. Since a high carrier density reduces the index of refraction, a competing antiguiding effect can occur. For index guiding, the lateral light confinement is caused by a lateral increase of the index of refraction. This index modulation can be achieved by using a mesa-like contact stripe (Fig. 23.41a). A shallow mesa reaches down into the upper cladding, a deep mesa reaches down into or through the active layer. Possible problems with surface recombination can be avoided by regrowth of the structure (Fig. 23.41b) with a wide band gap material (compared to the active layer). Optimization of regrowth is targeted to achieve a well-defined surface for subsequent contact processing. A lateral pn-diode can be incorporated that avoids current spreading in the upper part of the structure.

Depending on the width of the lateral mode, it can be monomode or multimode (Fig. 23.42a, b). For laterally monomode lasers, the stripe width may only be a few μm. In particular for such lasers, the current spreading must be controlled. Problems can arise for wide stripe widths due to current filamentation and inhomogeneous laser emission from the facet. Since the optical mode is typically more confined in the growth direction than in the lateral direction, the far field is asymmetric (Fig. 23.43a, b). The vertical axis has the higher divergence and is called the fast axis. The lateral axis is called the slow axis. The asymmetric beam shape is detrimental when the laser needs to be coupled into an optical fiber or a symmetric beam profile is needed for subsequent optics. The beam can be made symmetric using special optic components such as anamorphic prisms (Fig. 23.43c) and graded-index lenses. The beam from a laterally monomode laser is diffraction limited and can therefore generally be refocused efficiently (beam quality $M^2 \gtrsim 1$).

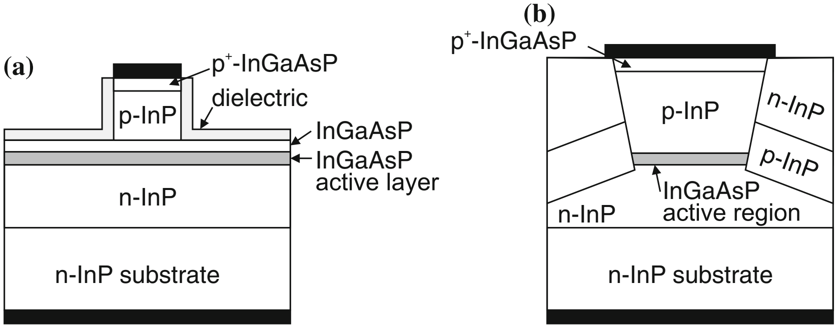

Fig. 23.41 Schematic cross section of index-guided lasers: (**a**) shallow ridge, (**b**) deep etch and regrowth. *Black areas* are metal contacts

Fig. 23.42 Lateral near field (**a**) and far field (**b**) of lasers with various width *S* of the injection stripe as labeled. Adapted from [1685]

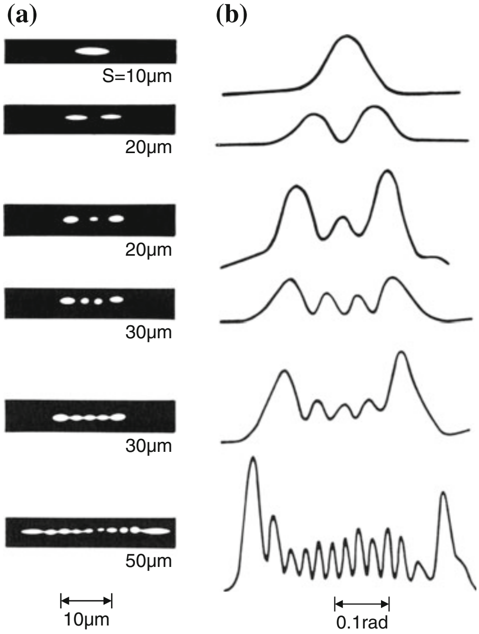

Longitudinal Modes

The spectral positions of the laser modes for a cavity with length L is given by the condition (cf. (19.34))

$$L = \frac{m\,\lambda}{2\,n_{\mathrm{r}}(\lambda)}, \tag{23.16}$$

where m is a natural number and $n(\lambda)$ is the dispersion of the index of refraction. The distance of neighboring modes is given by (for large m)

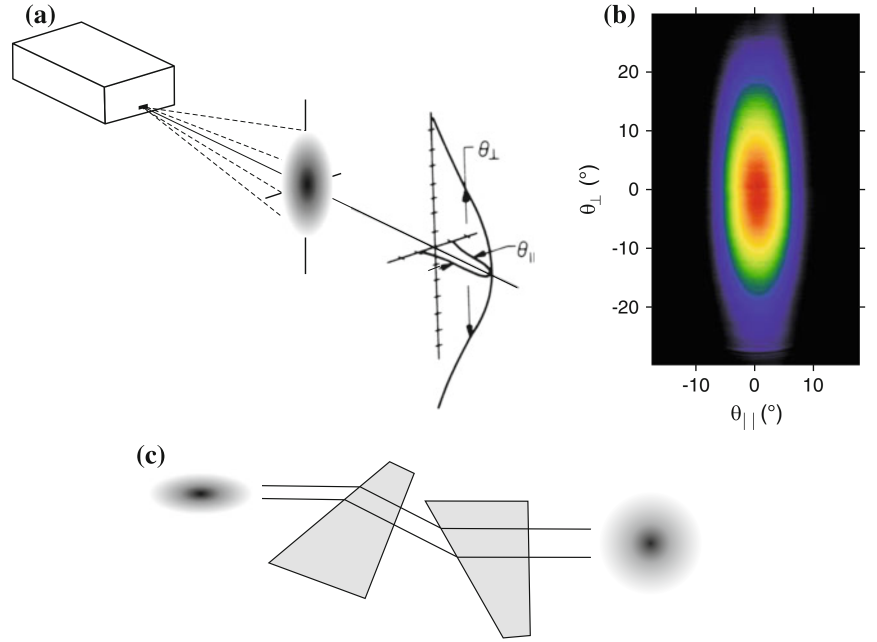

Fig. 23.43 (**a**) Schematics of the asymmetric far field of an edge emitter. Adapted from [500]. (**b**) Far-field distribution of violet GaN-based laser. Adapted from [1686]. (**c**) Correction of asymmetric far field with a pair of anamorphic prisms

$$\Delta\lambda = \frac{\lambda^2}{2\,n_\mathrm{r}\,L\left(1 - \frac{\lambda}{n_\mathrm{r}}\frac{\mathrm{d}n_\mathrm{r}}{\mathrm{d}\lambda}\right)}. \tag{23.17}$$

The dispersion $\mathrm{d}n_\mathrm{r}/\mathrm{d}\lambda$ can sometimes be neglected.

The facets of edge-emitting lasers are typically cleaved. Cleaving bears the danger of mechanical breakage and tends to have poor reproducibility, low yield and therefore high cost. Etched facets are another possibility to form the cavity mirror. The etch process, typically reactive ion dry etching, must yield sufficiently smooth surfaces to avoid scattering losses. A highly efficient distributed Bragg mirror (cf. Sect. 19.1.4) with only a few periods can be created by using the large index contrast between the semiconductor and air. As shown in Fig. 23.44, slabs can be etched that make a Bragg mirror with the air gaps [1687]. In this way, very short longitudinal cavities can be made (≈10 μm).

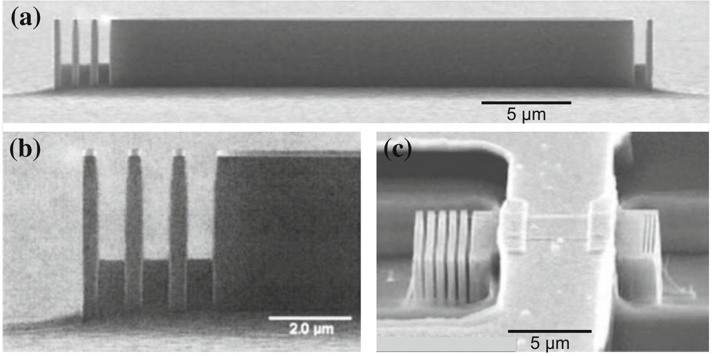

Fig. 23.44 SEM image of (**a**) an InP microlaser with third-order Bragg mirrors, (**b**) magnified view of the front facet with three slabs, (**c**) a 12 μm long microlaser with five third-order mirrors on the rear side and three first-order mirrors on the front side with top contact. From [1688]; part (**b**) reprinted with permission from [1687], © 2001 AIP

23.4.5 Loss Mechanisms

While the light travels through the cavity, it is not only amplified but it also suffers losses. The internal loss α_i and the mirror loss α_m contribute to the total loss α_tot

$$\alpha_\mathrm{tot} = \alpha_\mathrm{i} + \alpha_\mathrm{m}. \tag{23.18}$$

The internal loss is due to absorption in the cladding, scattering at waveguide inhomogeneities and possibly other processes. It can be written as

$$\alpha_\mathrm{i} = \alpha_0\, \Gamma + \alpha_\mathrm{g}\, (1 - \Gamma), \tag{23.19}$$

where α_0 is the loss coefficient in the active medium and α_g is the loss coefficient outside the active medium.

The mirror loss is due to the incomplete reflection of the optical wave at the laser facets. This condition is necessary, however, to observe a laser beam outside the cavity. R_1 and R_2 are the values of reflectance of the two facets, respectively. An as-cleaved facet has a reflectance of about 30 % (cf. (23.8)). Using dielectric layers on the facets, the reflectance can be increased (high reflection, HR-coating) or decreased (antireflection, AR-coating). One round-trip through the cavity of length L has the length $2L$. The intensity loss due to reflection at the facets is expressed via $\exp(-2\alpha_\mathrm{m} L) = R_1\, R_2$

$$\alpha_\mathrm{m} = \frac{1}{2L} \ln\left(\frac{1}{R_1\, R_2}\right). \tag{23.20}$$

If both mirrors have the same reflectance R, we have $\alpha_{\mathrm{m}} = -L^{-1} \ln R$. For $R = 0.3$ a 1 mm cavity has a loss of $12\,\mathrm{cm}^{-1}$. For the internal loss a typical value is $10\,\mathrm{cm}^{-1}$, very good waveguides go down to 1–$2\,\mathrm{cm}^{-1}$.

Lasing is only possible if the gain overcomes all losses (at least for one wavelength), i.e.

$$g_{\mathrm{mod}} = g_{\mathrm{mat}}\, \Gamma \geq \alpha_{\mathrm{tot}}. \tag{23.21}$$

23.4.6 Threshold

When the laser reaches threshold, the (material) gain is pinned at the threshold value

$$g_{\mathrm{thr}} = \frac{\alpha_{\mathrm{i}} + \alpha_{\mathrm{m}}}{\Gamma}. \tag{23.22}$$

Since $g \propto n$, the carrier density is also pinned at its threshold value and does not increase further with increasing injection current. Instead, additional carriers are quickly converted into photons by stimulated emission. The threshold carrier density is (using the linear gain model, cf. (23.13))

$$n_{\mathrm{thr}} = n_{\mathrm{tr}} + \frac{\alpha_{\mathrm{i}} + \alpha_{\mathrm{m}}}{\hat{\alpha}\, \Gamma}. \tag{23.23}$$

For an active layer of thickness d, the threshold current density is

$$j_{\mathrm{thr}} \cong \frac{e\, d\, n_{\mathrm{thr}}}{\tau(n_{\mathrm{thr}})}, \tag{23.24}$$

where $\tau(n_{\mathrm{thr}})$ is the (minority) carrier lifetime at the threshold carrier density (cmp. Sect. 10.10) from

$$\tau(n) = \frac{1}{A + B\, n + C\, n^2}. \tag{23.25}$$

Using (23.23), we can write (for $R = R_1 = R_2$)

$$j_{\mathrm{thr}} = j_{\mathrm{tr}} + \frac{e\, d}{\tau\, \hat{\alpha}\, \Gamma} \left(\alpha_{\mathrm{i}} - \frac{1}{L} \ln R \right), \tag{23.26}$$

where the transparency current density is $j_{\mathrm{tr}} = e\, d\, n_{\mathrm{tr}}/\tau$. Thus, the plot of j_{thr} versus $1/L$ (or the optical loss) should be linear and can be extrapolated towards the transparency current density (cf. Fig. 23.45a).

Any additional increase of the current j leads to stimulated emission with the rate

$$r_{\mathrm{st}} = d\, v_{\mathrm{g}}\, g_{\mathrm{thr}}\, N_{\mathrm{ph}}, \tag{23.27}$$

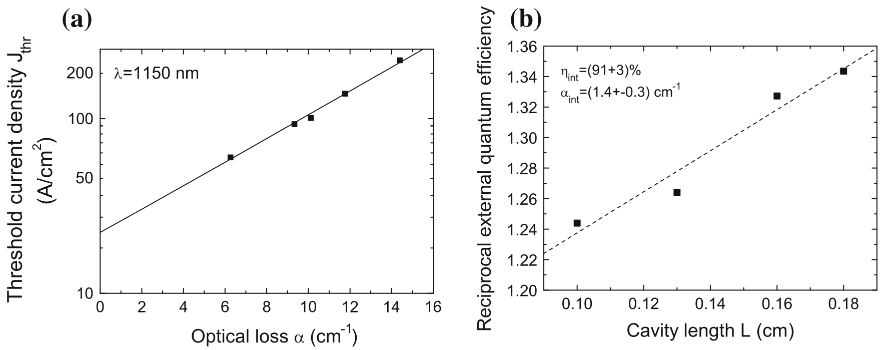

Fig. 23.45 (**a**) Threshold current density for (three-fold InGaAs/GaAs QD stack) laser ($\lambda = 1150\,\mathrm{nm}$) at 10 °C with different cavity length versus the optical loss ($\propto 1/L$). The extrapolated transparency current density is $21.5 \pm 0.9\,\mathrm{A/cm^2}$. (**b**) Inverse external quantum efficiency versus cavity length. The internal quantum efficiency determined from the plot is 91 % and the internal loss is $1.4\,\mathrm{cm}^{-1}$

where v_g is the group velocity (mostly c_0/n_r) and N_ph is the photon density (per length) in the cavity. The photon density increases linearly beyond the threshold

$$N_\mathrm{ph} = \frac{1}{e\,d\,v_\mathrm{g}\,g_\mathrm{thr}}\,(j - j_\mathrm{thr})\,. \tag{23.28}$$

The photon lifetime

$$\frac{1}{\tau_\mathrm{ph}} = v_\mathrm{g}\,(\alpha_\mathrm{i} + \alpha_\mathrm{m}) = v_\mathrm{g}\,\Gamma\,g_\mathrm{thr} \tag{23.29}$$

is introduced that describes the loss rate of photons. $v_\mathrm{g}\,\alpha_\mathrm{m}$ describes the escape rate of photons from the cavity into the laser beam(s). Therefore,

$$N_\mathrm{ph} = \frac{\tau_\mathrm{ph}\,\Gamma}{e\,d}\,(j - j_\mathrm{thr})\,. \tag{23.30}$$

Since the threshold depends on the carrier density, it is advantageous to reduce the active volume further and further. In this way, the same *amount* of injected carriers creates a larger carrier *density*. Figure 23.46 shows the historic development of laser threshold due to design improvements.

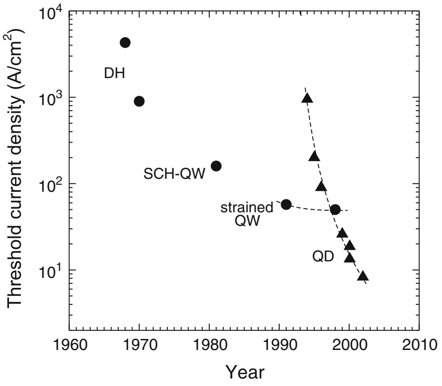

Fig. 23.46 Historic development of threshold current density (at room temperature, extrapolated for infinite cavity length and injection stripe width) for various laser designs, 'DH': double heterostructure, 'SCH–QW': separate confinement heterostructure with quantum wells. 'QD': quantum dots. *Dashed lines* are guides to the eye

23.4.7 Spontaneous Emission Factor

The spontaneous emission factor β is the fraction of spontaneous emission (emitted into all angles) that is emitted into laser modes. For Fabry–Perot lasers, β is typically in the order of 10^{-4}–10^{-5}. The design of a microcavity can increase β drastically by several orders of magnitude to ≈ 0.1 [1689] or above and thus reduce the threshold current. The photon number as a function of the pump current can be calculated from the laser rate equations and is depicted in Fig. 23.47. For $\beta = 1$, all emitted power goes into the laser mode regardless of whether emission is spontaneous or stimulated. The definition of threshold in such 'nonclassical' lasers with large β is discussed in detail in [1690].

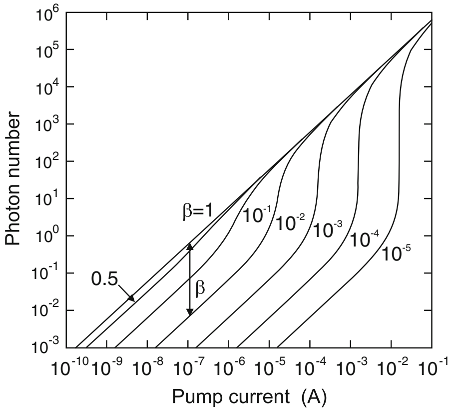

Fig. 23.47 Photon number versus pump current for a model laser. Adapted from [1691]

23.4.8 Output Power

The output power is given by the product of photon energy, the photon density in the cavity, the effective mode volume and the escape rate:

$$P_{\text{out}} = \hbar\omega\, N_{\text{ph}}\, \frac{L\, w\, d}{\Gamma}\, v_{\text{g}}\, \alpha_{\text{m}}. \tag{23.31}$$

Thus, it is given by

$$P_{\text{out}} = \hbar\omega\, v_{\text{g}}\, \alpha_{\text{m}}\, \frac{\tau_{\text{ph}}}{e}\, L\, w\, (j - j_{\text{thr}}) = \frac{\hbar\omega}{e}\, \frac{\alpha_{\text{m}}}{\alpha_{\text{m}} + \alpha_{\text{i}}}\, (I - I_{\text{thr}})\,. \tag{23.32}$$

To this equation, the factor η_{int} must be added. The internal quantum efficiency describes the efficiency of the conversion of electron–hole pairs into photons (cmp. (10.59)):

$$\eta_{\text{int}} = \frac{B\, n^2 + v_{\text{g}}\, g_{\text{thr}}\, N_{\text{ph}}}{A\, n + B\, n^2 + C\, n^3 + v_{\text{g}}\, g_{\text{thr}}\, N_{\text{ph}}}. \tag{23.33}$$

All in all, now (see Fig. 23.48a)

$$P_{\text{out}} = \frac{\hbar\omega}{e}\, \frac{\alpha_{\text{m}}}{\alpha_{\text{m}} + \alpha_{\text{i}}}\, \eta_{\text{int}}\, (I - I_{\text{thr}})\,. \tag{23.34}$$

The differential (or slope) quantum efficiency, also called the external quantum efficiency η_{ext}, is the slope of the P_{out} curve versus the current in the lasing regime. It is given by

$$\eta_{\text{ext}} = \frac{\mathrm{d}P_{\text{out}}/\mathrm{d}I}{\hbar\omega/e} = \eta_{\text{int}}\, \frac{\alpha_{\text{m}}}{\alpha_{\text{m}} + \alpha_{\text{i}}}. \tag{23.35}$$

The external quantum efficiency can also be written as

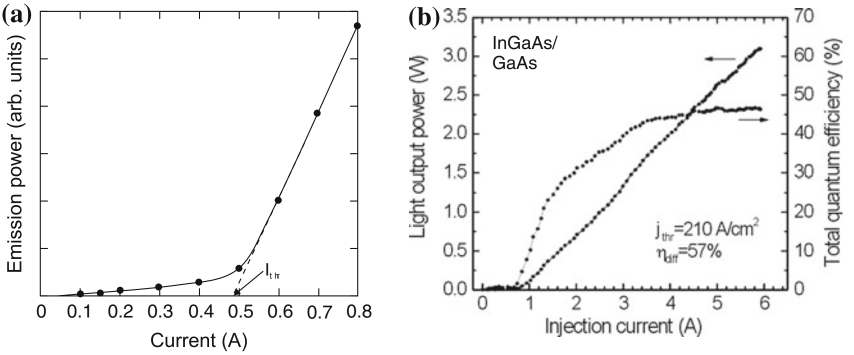

Fig. 23.48 (**a**) Typical P–I characteristic of a semiconductor laser. Adapted from [500]. (**b**) Output power and total quantum efficiency of a quantum dot laser (3 stacks of InGaAs/GaAs QDs, L = 2 mm, w = 200 μm, λ = 1100 nm, T = 293 K) versus injection current

$$\frac{1}{\eta_{\rm ext}} = \frac{1}{\eta_{\rm int}}\left(1 + \frac{\alpha_{\rm i}}{\alpha_{\rm m}}\right) = \frac{1}{\eta_{\rm int}}\left[1 - 2\alpha_{\rm i}\, L\, \ln\left(R_1 R_2\right)\right]. \tag{23.36}$$

Therefore, if $\eta_{\rm ext}^{-1}$ is plotted for similar lasers with different cavity length (see Fig. 23.45b), a straight line should arise from which the internal quantum efficiency (extrapolation to $L \to 0$) and the internal loss ($\propto$ slope) can be determined experimentally.

The threshold current for a given laser is determined from the P–I characteristic via extrapolation of the linear regime as shown in Fig. 23.48a. Record values for the threshold current density are often given for the limit $L \to \infty$. Due to current spreading, the threshold current density also depends on the width of the injection stripe. Record low thresholds are therefore often given for the limit $w \to \infty$.

The total quantum efficiency is given by

$$\eta_{\rm tot} = \frac{P_{\rm out}/I}{\hbar\omega/e}. \tag{23.37}$$

This quantity is shown in Fig. 23.48b for a laser as a function of the current. For a linear P–I lasing characteristic, the total quantum efficiency converges towards the external quantum efficiency for high currents because the low quantum efficiency subthreshold regime no longer plays any role. Another important figure of merit is the wall-plug efficiency $\eta_{\rm w}$ that describes the power conversion:

$$\eta_{\rm w} = \frac{P_{\rm out}}{U\, I}. \tag{23.38}$$

Additionally to the current balance discussed so far, typically a leakage current exists that flows without contributing to recombination or lasing. Carriers not captured into or escaping from the active layers can contribute to this current. The present record for wall-plug efficiency of high-power laser diodes is above 70 % [1692, 1693], employing careful control of band alignment (graded junctions, avoiding voltage barriers), optical losses, Joule heating, spontaneous emission and carrier leakage. It seems possible to achieve $\eta_{\rm w}$ of 80 %.

The P–I characteristic is not linear to arbitrary high currents. Generally, the output power will saturate or even decrease for increasing current. These effects can be due to increasing leakage current, increasing internal loss at high current or temperature effects, e.g. an increase of threshold with increasing temperature (cf. Sect. 23.4.9) and therefore a reduction of total efficiency. All nonradiative losses will eventually show up as heat in the laser that must be managed with a heat sink.

A radical effect is catastrophical optical damage (COD) at which the laser facet is irreversible (partially) destructed. Antioxidation or protective layers can increase the damage threshold to >20 MW/cm^2. The record power from a single edge emitter is ~12 W (200 µm stripe width). For a lateral monomode laser, cw power of about 1.2 W has been reached from a 1480 nm InGaAsP/InP double quantum-well lasers with 3–5 μm stripes and 3 mm cavity length [1694]. About 500 mW can be coupled into a single-mode fiber [1695].

23.4.9 Temperature Dependence

The threshold of a laser typically increases with increasing temperature as shown in Fig. 23.49a. Empirically, in the vicinity of a temperature T_1 the threshold follows an exponential law (see Fig. 23.49b)

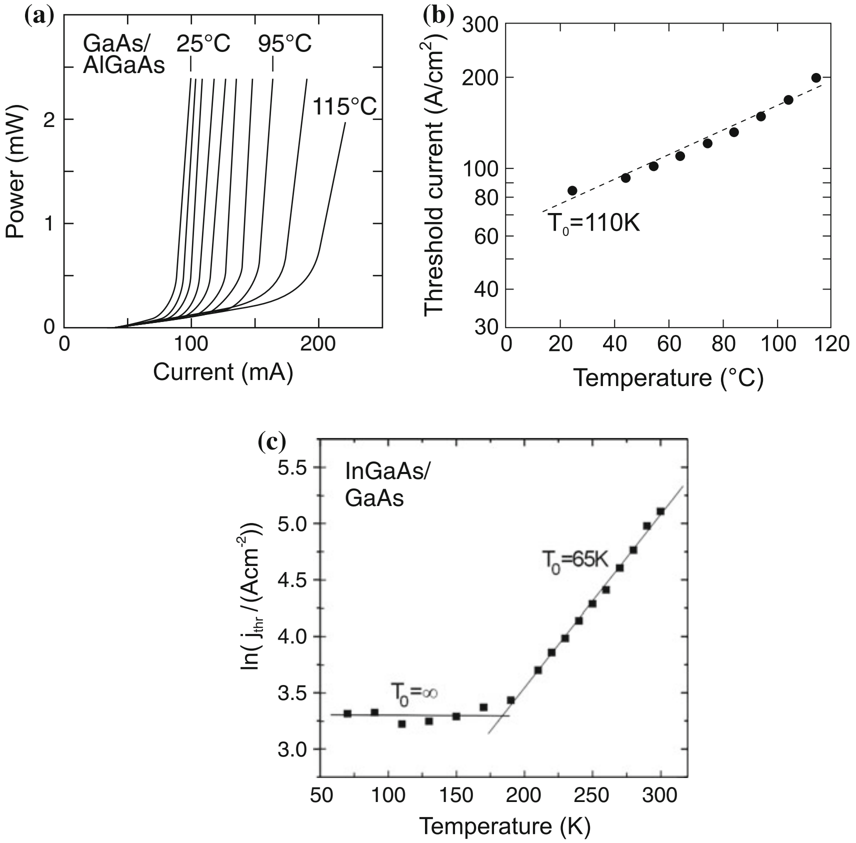

Fig. 23.49 (**a**) *P–I* characteristic (cw output power per mirror facet) of stripe-buried heterostructure laser at various temperatures of the heat sink between 25 °C and 115 °C in steps of 10 K. (**b**) Threshold current (in logarithmic scale) of this laser as a function of heat-sink temperature and exponential fit (*dashed line*) with $T_0 = 110\,\mathrm{K}$. Parts (**a**) and (**b**) adapted from [1696]. (**c**) Temperature dependence of the threshold current density of a quantum dot laser (3 stacks of InGaAs/GaAs QDs, $\lambda = 1150\,\mathrm{nm}$) with T_0 (*solid lines* are fits) given in the figure

$$j_{\mathrm{thr}}(T) = j_{\mathrm{thr}}(T_1)\ \exp\left(\frac{T - T_1}{T_0}\right) \propto \exp\left(\frac{T}{T_0}\right), \tag{23.39}$$

with T_0 being the so-called characteristic temperature.[20] It is the inverse logarithmic slope, $T_0^{-1} = \mathrm{d} \ln j_{\mathrm{thr}} / \mathrm{d}T$.

T_0 summarizes the temperature-dependent loss and the carrier redistribution in **k**-space due to the change of the Fermi distribution with temperature. With increasing temperature, populated states below the quasi-Fermi level become unpopulated and nonlasing states become populated. Therefore, the gain decreases with increasing temperature. This redistribution must be compensated by an increase of the quasi-Fermi energy, i.e. stronger pumping. This effect is present for (even ideal) bulk, quantum well and quantum wire lasers. Only for quantum dots with a δ-like density of states is the change of Fermi distribution irrelevant as long as excited states are energetically well separated from the (lasing) ground state. In Fig. 23.49c, the threshold of a quantum dot laser is indeed temperature independent ($T_0 = \infty$) as long as excited states are not thermally populated (for $T < 170\,\mathrm{K}$ for the present laser).

23.4.10 Mode Spectrum

In Fig. 23.50a, the mode spectrum of a typical edge-emitting laser is shown. Below threshold, the amplified spontaneous emission (ASE) spectrum exhibits a comb-like structure due to the Fabry–Perot modes. Above threshold, some modes grow much faster than others, possibly resulting in single longitudinal mode operation at high injection. The relative strength of the strongest side mode is expressed through the side-mode suppression ratio (SSR) in dB

$$SSR = 10\ \log\left(\frac{I_{\mathrm{mm}}}{I_{\mathrm{sm}}}\right), \tag{23.40}$$

where I_{mm} (I_{sm}) is the intensity of the maximum (strongest side) mode in the lasing spectrum.

As a tendency a DHS or QW semiconductor laser above threshold develops a narrow spectrum since the pump power is channeled into one or few modes with large gain. A quantum dot laser behaves differently when pumped largely above threshold. Since the gain of individual QDs in an inhomogeneously broadened ensemble (due to different QD sizes) is independent, a broad gain spectrum is present [1699]. The lasing spectrum takes a hat-like shape when homogeneous broadening is small compared to the inhomogeneous broadening [1698, 1700] (Fig. 23.51) as predicted theoretically [1699, 1701].

---

[20] Since T_0 has the dimension of a temperature difference, it can be expressed in °C or K. For the sake of unambiguity it should be given in K.

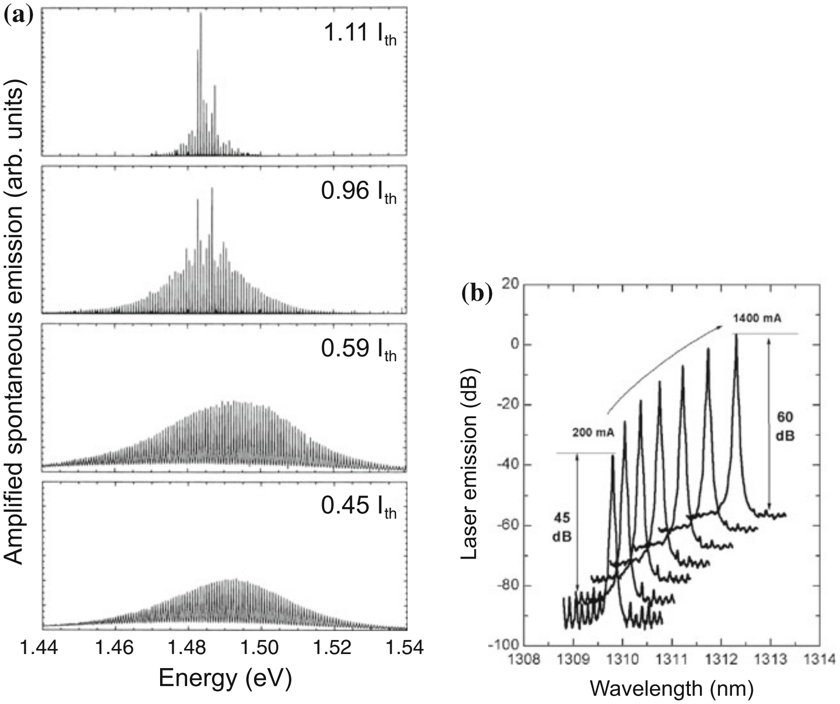

Fig. 23.50 (**a**) Mode spectra of a Fabry–Perot laser, under, at and above threshold ($I_{\mathrm{thr}} = 13.5\,\mathrm{mA}$). Adapted from [1047]. (**b**) Mode spectra of a cw DFB InGaAs/InP laser with 2 mm cavity length at various currents of 200, 400, ..., 1400 mA ($I_{\mathrm{thr}} = 65\,\mathrm{mA}$), SSR $> 40\,\mathrm{dB}$ at $T = 293\,\mathrm{K}$. Adapted from [1697], reproduced with permission from SPIE

23.4.11 Longitudinal Single-Mode Lasers

In order to achieve a high SSR or single longitudinal mode lasing, the feedback must offer a higher wavelength selectivity than a simple mirror. A preferential feedback for certain modes can be obtained using a periodic dielectric structure that 'fits' to a particular wavelength, similar to a Bragg mirror. The periodic modulation of the refractive index can be made within the cavity (distributed feedback, DFB, Fig. 23.52a) or at the mirror (distributed reflection, DBR, Fig. 23.52b). In this way, monochromatic lasers with SSR $\gg$30 dB are possible (Fig. 23.50b).

It is possible to couple several hundred mW optical power of a laterally and spectrally monomode laser into a monomode optical fiber [1702] (Fig. 23.53).

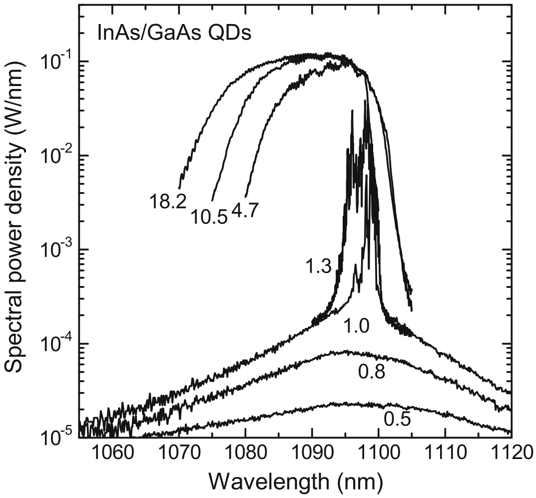

Fig. 23.51 Lasing spectra of quantum dot laser ($L = 1.2\,\mathrm{mm}$, stripe width $w = 75\,\mu\mathrm{m}$) at room temperature. The active medium is a three-fold stack of InGaAs/GaAs QDs. The current density as labeled is given in units of the threshold current density ($j_{\mathrm{thr}} = 230\,\mathrm{A/cm}^2$). Adapted from [1698]

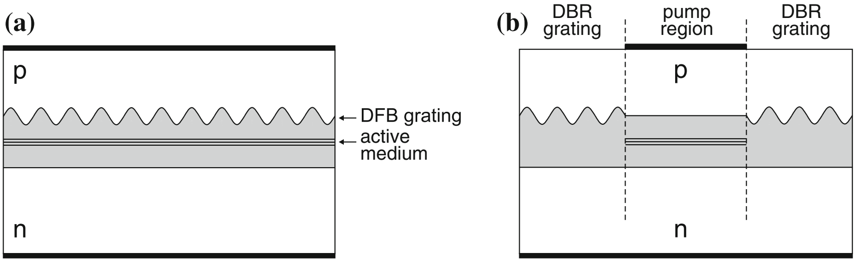

Fig. 23.52 Schematic drawing of (**a**) DFB (distributed feedback) and (**b**) DBR (distributed Bragg reflection) lasers. The active medium is schematically shown as a triple quantum well, the waveguide is shown as a *grey area*

23.4.12 Tunability

The tunability of the emission wavelength [1704] is important for several applications such as wavelength division multiplexing[21] and spectroscopy.

The simplest possibility to tune a laser is to vary its temperature and thus its band gap. This method is particularly used for lead salt lasers in the mid-infrared region,[22] as shown in Fig. 23.54.

---

[21] In order to make better use of the high bandwidth of the optical fiber several information channels with closely lying wavelengths are transmitted.

[22] Note the anomalous positive coefficient $\mathrm{d}E_{\mathrm{g}}/\mathrm{d}T$ as discussed in Sect. 6.7.

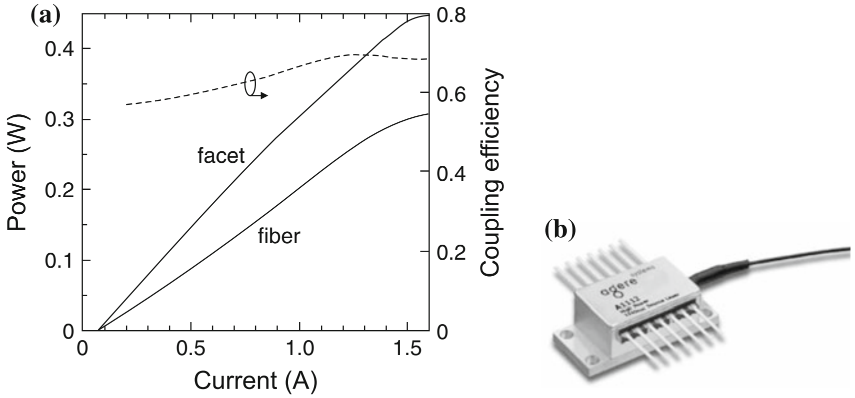

Fig. 23.53 (**a**) Output power of an InGaAsP/InP cw single-mode DFB laser at 1427 nm with 2 mm cavity length from the facet and coupled to a single-mode fiber versus driving current ($T = 293$ K). The *dashed* line represents the coupling efficiency to the fiber (right scale). Adapted from [1702]. (**b**) Package with pigtail of fiber coupled 1550 nm DFB laser with 40 mW output power in the fiber. From [1703]

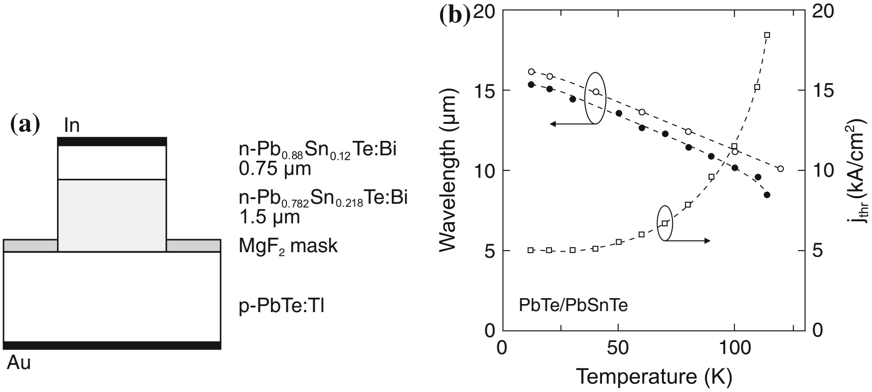

Fig. 23.54 (**a**) Schematic drawing of PbTe lead salt laser. (**b**) Tuning characteristics of such laser: Emission wavelength (*left scale*, *filled circles*: emission wavelength at cw threshold, *empty circles*: emission maximum under pulsed operation) and cw threshold current density (*right scale*) as a function of the heat-sink temperature. *Symbols* are experimental data, *dashed lines* are guides to the eye. Adapted from [1705]

For monomode lasers, mode hopping, i.e. the discontinuous shift of lasing wavelength (or gain maximum) from one mode to the next, poses a problem for continuous tuning, as shown in Fig. 23.55. The continuous shift of emission wavelength is due to the temperature dependence of the index of refraction and subsequently the longitudinal modes. The index of refraction increases with increasing temperature at typically $\sim 3 \times 10^{-4}\,\mathrm{K}^{-1}$. Generally, a red-shift is the consequence.

Fig. 23.55 Wavelength as a function of temperature (with mode hopping) for a GaAs-based DFB laser

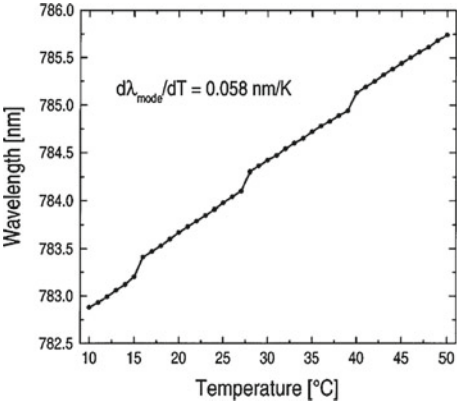

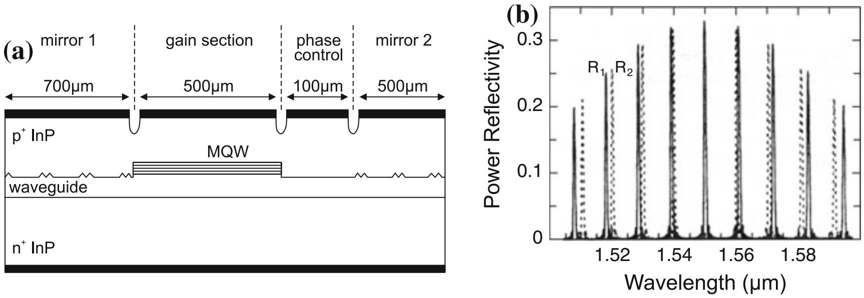

Fig. 23.56 (**a**) Schematic representation of SGDBR (sampled-grating DBR) laser with four sections. Adapted from [1706]. (**b**) Reflectance of two sampled gratings DBR mirrors

Another possibility to vary the index of refraction (and thus the optical path length) is a variation of the carrier density. The coefficient $\mathrm{d}n_\mathrm{r}/\mathrm{d}n$ is about $-10^{-20}\,\mathrm{cm}^3$. In a two-section laser, separate regions (with separately controlled currents) for gain and tuning are present. The regions are separated with deep-etched trenches to avoid crosstalk. The tuning range is limited to about 10 nm. For a mode-hopping free tuning, the control of the phase in the cavity is important and requires an additional section for the phase control. Such a three-section laser has separate regions (and current control) for the reflection, phase and amplification (or gain) region.

Using sampled gratings, the tuning range can be strongly increased to about 100 nm. A sampled grating is a nonperiodic lattice that has several ($\sim$10) reflection peaks. The laser structure has four sections (Fig. 23.56) with two mirrors that have slightly different sampled gratings. Via the carrier densities in the two mirror sections, different maxima can be brought to overlap (Vernier effect) and the position of the selected maximum can be tuned over a wide spectral range (Fig. 23.57).

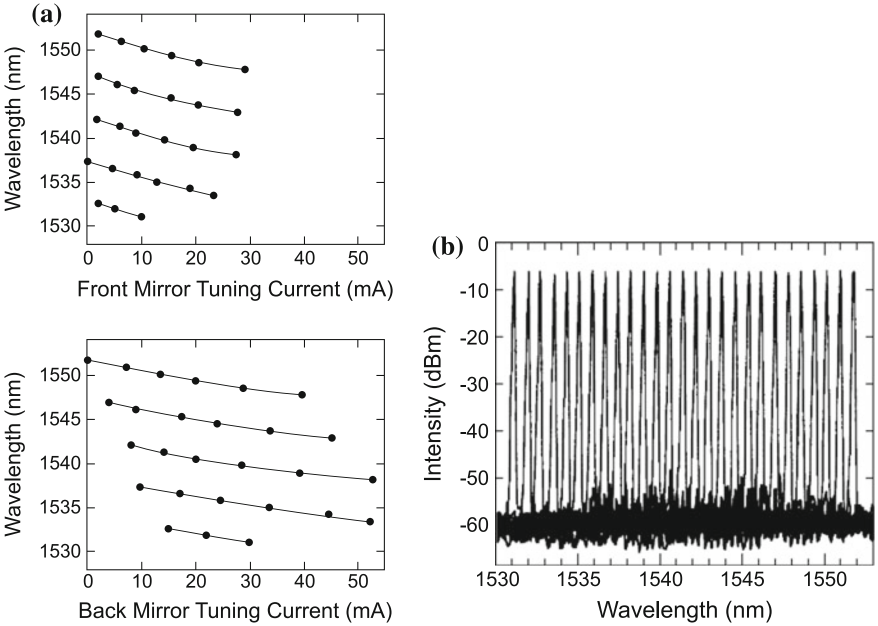

Fig. 23.57 (**a**) Tuning curves of two sampled gratings DBR mirrors for the front and back mirror current. (**b**) 27 wavelength channels (1531.12–1551.72 nm) with a channel separation of 1 nm. Adapted from [1707]

23.4.13 *Dynamics and Modulation*

For transmission of information in the time domain, the laser intensity must be modulated. This can be accomplished by *direct* modulation, i.e. modulation of the injection current, or *external* modulators, for example using the voltage-induced shift of the absorption spectrum due to QCSE (cf. Sect. 13.1.2). For direct modulation, small- and large-signal modulation are distinguished. A detailed treatment of laser dynamics and modulation can be found in [1708].

Laser Dynamics

The dynamical properties of the laser are described by the coupled rate equations for the carrier density n and the photon density (per volume) S:

$$\frac{\mathrm{d}n}{\mathrm{d}t} = \frac{j}{e\,d} - \frac{n}{\tau(n)} - g(n,S)\,v_\mathrm{g}\,S \tag{23.41a}$$

$$\frac{\mathrm{d}S}{\mathrm{d}t} = \Gamma\,g(n,S)\,v_\mathrm{g}\,S + \beta\,B\,n^2 - \frac{S}{\tau_\mathrm{ph}}. \tag{23.41b}$$

The first term in (23.41a) describes the electrical injection[23] ($=I/(e\,V)$), the second one the recombination (all channels) and the third one the carrier conversion to photons through stimulated emission via the gain g. In the photon dynamics (23.41b), the first term represents the gain term, the second one the photons in the laser mode from the recombination (spontaneous emission, cmp. Sect. 23.4.7) and the third term the photon loss (due to internal losses and the mirrors). The recombination rate $n/\tau(n)$ is typically given by (23.25). The photon lifetime τ_{ph} is given by (23.29). For the gain various models are used, a simple one being (cmp. (23.13)):

$$g(n, S) = g' \, \frac{n - n_{\mathrm{thr}}}{1 + \epsilon_S \, S}, \tag{23.42}$$

g' being the differential gain and ϵ_S being the gain compression coefficient due to spectral hole burning.

Large-Signal Modulation

If a current pulse is fed to the laser, the laser radiation is emitted with a short time delay, the so-called turn-on delay (TOD) time. This time is needed to build up the carrier density for inversion. The time dependence of the density is (neglecting the density dependence of the lifetime)

$$n(t) = \frac{I\,\tau}{e\,A\,d} \left[1 - \exp\left(-\frac{t}{\tau} \right) \right]. \tag{23.43}$$

The TOD time to reach the threshold density (using (23.24)) is

$$\tau_{\mathrm{TOD}} = \tau \, \ln \left(\frac{I}{I - I_{\mathrm{thr}}} \right). \tag{23.44}$$

We note that $\tau_{\mathrm{TOD}} > 0$ for $I > I_{\mathrm{thr}}$. Such a dependence is found experimentally (Fig. 23.58). The turn-on delay time decreases with increasing pump current but typically is at least 1 ns. In order to circumvent this limitation for more than about 1 GHz pulse repetition rate, the laser is biased slightly below threshold.

In Fig. 23.59a, the response (light emission) of a LED to a short current pulse is shown schematically. The monotonously decreasing transient (that is more or less exponential) corresponds to the carrier recombination dynamics. When a laser is excited with a steep (long) current pulse, the response exhibits so-called relaxation oscillations (RO) before the steady-state (cw) intensity level is reached (Fig. 23.59b).

In the laser, first the carrier density is built up. It surpasses the threshold density that leads to a build-up of the photon density. The laser pulse depletes the carrier density faster below threshold than the current can supply further carriers. Therefore, the laser intensity drops below the cw level. From the solution of the coupled rate equations for the electron and photon densities n and S (23.41a, b), the frequency of the relaxation oscillations is found as

---

[23] This term can be multiplied by the injection efficiency η_{inj} to account for leakage currents.

Fig. 23.58 Variation of turn-on delay time with the injected current for a laser at room temperature. Adapted from [1709]

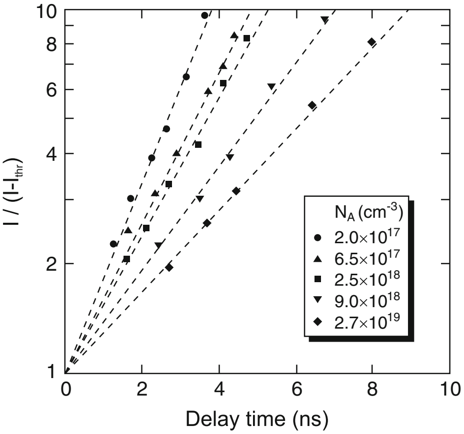

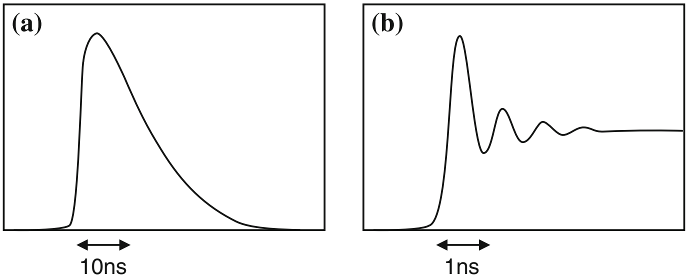

Fig. 23.59 Schematic response of (**a**) LED to current pulse and (**b**) of laser to current step

$$f_{\mathrm{RO}} = \frac{1}{2\pi} \left(\frac{v_{\mathrm{g}}\, g'\, S_0}{\tau_{\mathrm{ph}}} \right)^{1/2}, \tag{23.45}$$

where g' is the differential gain as defined in (23.42) and S_0 is the steady-state photon density per volume that is proportional to the laser power P. The dependence $f_{\mathrm{RO}} \propto S_0^{1/2}$ is also found experimentally (Fig. 23.60a). For higher power the relation $f_{\mathrm{RO}}^2 \propto S_0$ becomes non-linear (Fig. 23.60b) due to gain compression; in this case S_0 is replaced with $S_0/(1+\epsilon_S\, S_0) \propto P/(1+P/P_{\mathrm{sat}})$, with P_{sat} being the saturation power.

Pattern Response

For digital data transmission, the laser is driven with pulse sequences (bit patterns). The response to a random bit pattern is called an 'eye pattern' and is shown in Fig. 23.61. The pattern consists of traces of the type shown in Fig. 23.59b. A clear distinction with well-defined trigger thresholds between 'on'- and 'off'-states can only be made if the eye formed by the overlay of all possible traces remains open. From the eye patterns in Fig. 23.61, it can be seen that the RO overshoot can be suppressed by driving the laser with a dc offset current well above threshold.

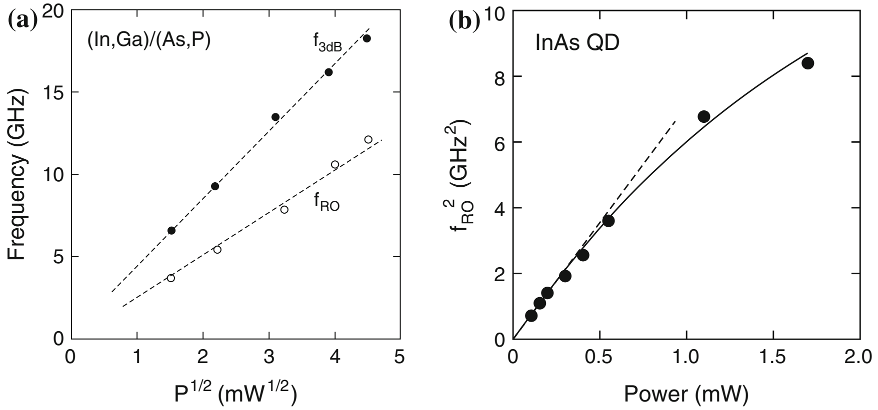

Fig. 23.60 (**a**) Dependence of small-signal 3 dB cutoff frequency f_{3dB} (*filled symbols*) and relaxation oscillation frequency f_{RO} (*empty symbols*) on the square root of the output power P for a DFB-laser. Adapted from [1710]. (**b**) Relaxation oscillation frequency f_{RO}^2 versus power for an InAs/GaAs QD laser. The *solid line* is a model including gain compression ($P_{sat} = 3.3$ mW), the *dashed line* is the linear relation (23.45) for small power. Adapted from [1711]

Fig. 23.61 Eye pattern of a single-mode VCSEL in response to a 10 Gb/s random bit pattern. The patterns are measured (**a**) with an offset current well above threshold and (**b**) with an offset current above but close to threshold. Adapted from [1712]

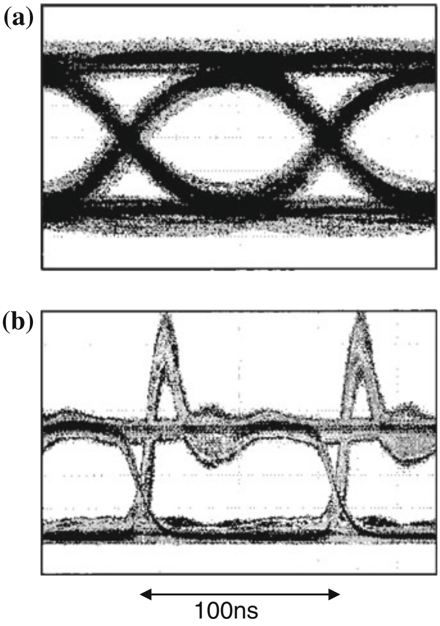

Small-Signal Modulation

In small-signal modulation, the injection current I is varied periodically by a small amount δI with $\delta I \ll I$ in the lasing regime. The current modulation leads to a corresponding variation of the output intensity. The frequency response is limited by the differential gain and the gain compression coefficient. The frequency response shifts to higher frequency with increasing laser power as shown in Fig. 23.62b.

α Factor

Another important quantity is the α factor, also called the linewidth enhancement factor [1713, 1714]. Due to the coupling of amplitude and phase fluctuations in the laser, the linewidth Δf is larger than expected.

$$\Delta f = \frac{\hbar\omega\, v_{\mathrm{g}}\, R_{\mathrm{spont}}\, \ln R}{8\pi\, P_{\mathrm{out}}\, L}(1+\alpha^2). \tag{23.46}$$

The linewidth enhancement is described via $(1+\alpha^2)$ with

$$\alpha = \frac{\mathrm{d}n_{\mathrm{r}}/\mathrm{d}n}{\mathrm{d}\kappa/\mathrm{d}n} = -\frac{4\pi}{\lambda}\frac{\mathrm{d}n_{\mathrm{r}}/\mathrm{d}n}{g'}, \tag{23.47}$$

where κ denotes the imaginary part of the index of refraction (9.4). Typical values for α are between 1 and 10. The linewidth is inversely proportional to the output power (Fig. 23.63).

23.4.14 Surface-Emitting Lasers

Surface-emitting lasers emit their beam normal to the surface. They can be fabricated from horizontal (edge-) emitters by reflecting the beam with a suitable mirror into the surface direction. This technology requires tilted facets or micro-optical components but allows for high power per area. In Fig. 23.64, a schematic cross section of a horizontal-cavity surface-emitting laser (HCSEL) and the light emission from an

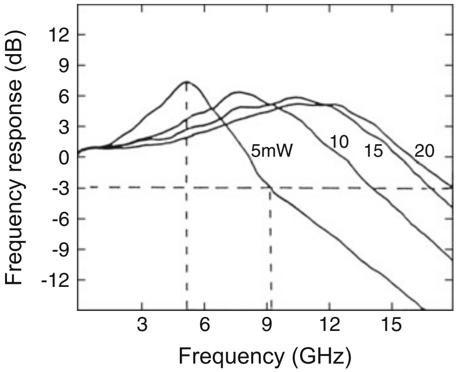

Fig. 23.62 Frequency response of a DFB-laser for various output powers as labeled. Adapted from [1710]

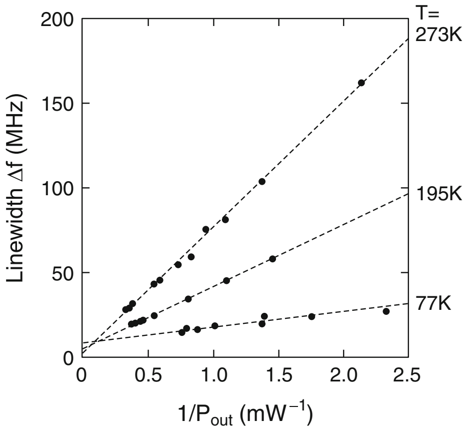

Fig. 23.63 Linewidth Δf of a cw GaAs/AlGaAs laser diode at various temperatures as a function of the inverse output power P_{out}^{-1}. At room temperature $\alpha \approx 5$. Adapted from [1715]

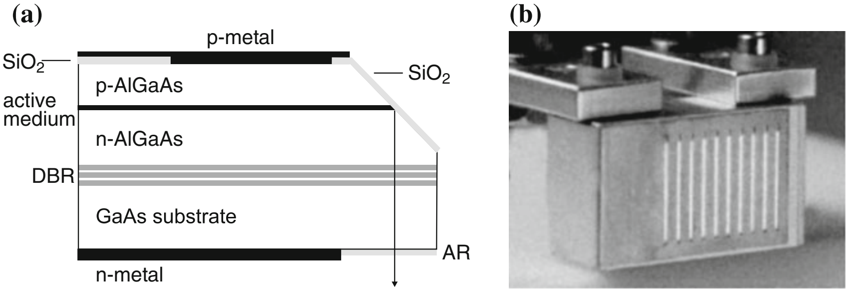

Fig. 23.64 (**a**) Principle of a surface-emitting laser. Light generated in the active region is internally reflected by the 45° angled mirror and directed through the substrate; 'AR': antireflection coating, 'DBR': epitaxial Bragg mirror. (**b**) Light emission from a 10 × 22 surface-emitting diode array. The light emission appears as stripes due to the broad beam divergence in the vertical direction. Part (**b**) reprinted with permission from [1716]

array of 220 such lasers are shown. The laser contains a 45° mirror that steers the light through the substrate and a Bragg mirror to provide the cavity mirror. The facet can also be fabricated such that the emission is to the top surface (Fig. 23.65). Another possibility to couple the beam out of a horizontal cavity is a surface grating.

Now, surface-emitting lasers with vertical-cavity (VCSEL), as shown in Fig. 23.29b, will be discussed. A detailed treatment can be found in [1718]. VCSELs are of increasing importance after many issues regarding their technology and fabrication have been solved. VCSEL fabrication is essentially a planar technology and VCSELs can be fabricated as arrays (Fig. 23.67). An on-wafer test of their properties is possible. They offer a symmetrical (or possibly a controlled asymmetrical) beam profile (Fig. 23.66) with possible polarization control or fixation.

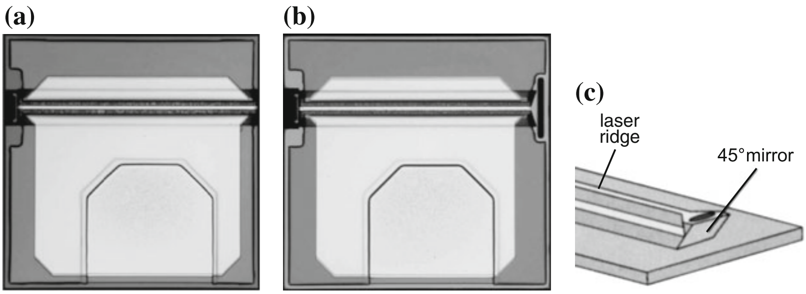

Fig. 23.65 (**a**) Horizontal Fabry–Perot cavity InP-based laser with 1310 nm emission length and 10 mW output power for modulation at 2.5 GB/s. The right facet is formed as DBR, emission is to the left. The trapezoid area in the center bottom of the image is the bond pad for the top contact. (**b**) Horizontal-cavity surface-emitting laser. Compared to (**a**), the right facet is replaced with a 45° mirror, leading to surface emission. (**c**) Schematic drawing of the tilted facet. Parts (**a**) and (**b**) from [1717]

Fig. 23.66 In-plane near field of a VCSEL with 6 μm oxide aperture at various currents, (**a**) 3.0 mA, (**b**) 6.2 mA, (**c**) 14.7 mA, (**d**) 18 mA

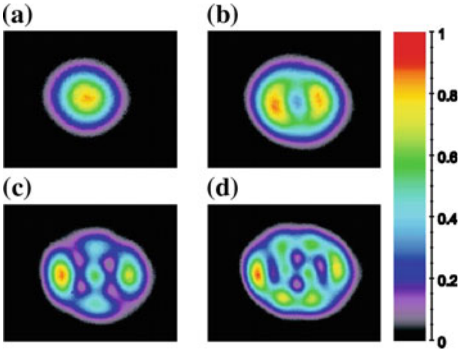

The cavity is formed by two highly reflecting Bragg mirrors with a distance of $\lambda/2$ or $3\lambda/2$ forming a microcavity (see Sect. 19.1.7). A high index contrast can be obtained from GaAs/AlAs Bragg mirrors in which the AlAs layers have been selectively oxidized in a hot moist atmosphere. Pure semiconductor Bragg mirrors suffer typically from small index contrast and require many pairs. This poses a problem, e.g. for InP-based VCSELs. In Fig. 23.68, the distribution of light intensity along a $3\lambda/2$ cavity is shown. In the stop band of the mirrors, there is only one optical mode, the cavity mode, that can propagate along the vertical (z) direction.

The current path through the active layer can be defined with an oxide aperture. This aperture is fabricated by selective oxidation of an AlAs layer, leaving a circular opening in the center of the VCSEL pillar as shown in Fig. 23.69. The current can be injected through the mirrors if they are doped. Alternatively, the current can be directly fed to the active layer by so-called intracavity contacts.

The emission wavelength of a VCSEL can be shifted via a variation of temperature or pump power. Tuning of the VCSEL emission can also be accomplished by leaving an air gap between the cavity and the upper mirror [1722]. Applying a voltage to the

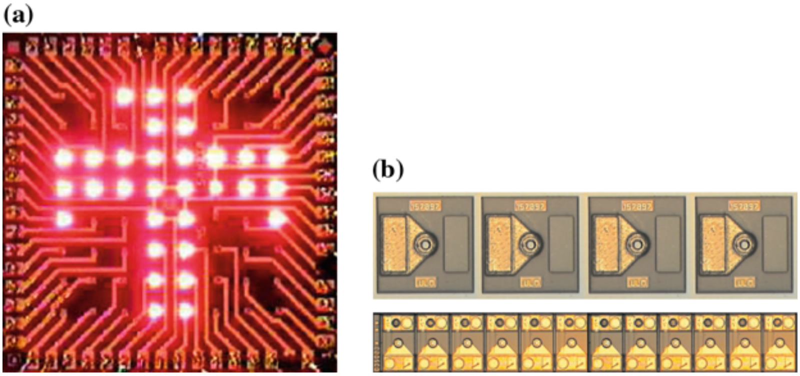

Fig. 23.67 (**a**), (**b**) VCSEL arrays. Part (**a**) reprinted from [1719] with permission, part (**b**) reprinted from [1720] with permission

Fig. 23.68 Simulation of the longitudinal distribution of the optical field in a VCSEL structure. The active medium are five quantum wells in the center. Reproduced from [1721] by permission from the MRS Bulletin

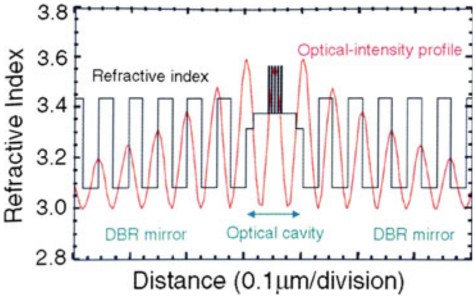

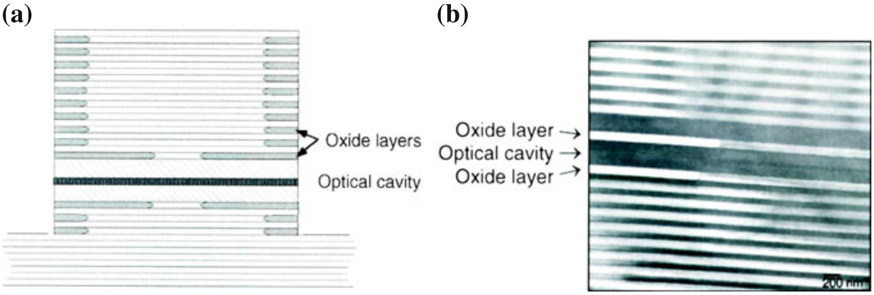

Fig. 23.69 (**a**) Schematic cross section of VCSEL with oxide aperture, (**b**) TEM image of cross section. Reproduced from [1721] by permission from the MRS Bulletin

lever arm with the top mirror, the width of the air gap can be varied. This variation leads to a shift of the cavity mode and therefore of the laser emission wavelength (Fig. 23.70). A VCSEL with air gap and particularly a high contrast Bragg mirror is achieved with InP/air as shown in Fig. 23.71.

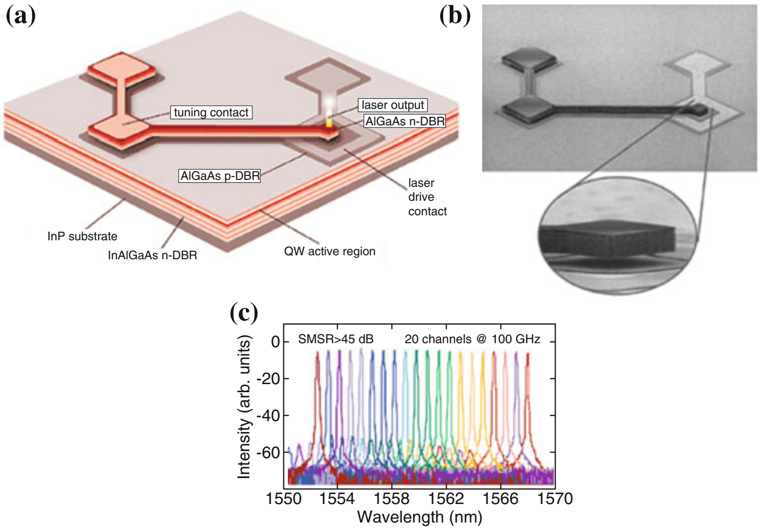

Fig. 23.70 (**a**) Schematic setup and (**b**) SEM image of VCSEL with air gap between active layer and top Bragg mirror, (**c**) spectra for different tuning conditions (via the width of the air gap). From [1723]

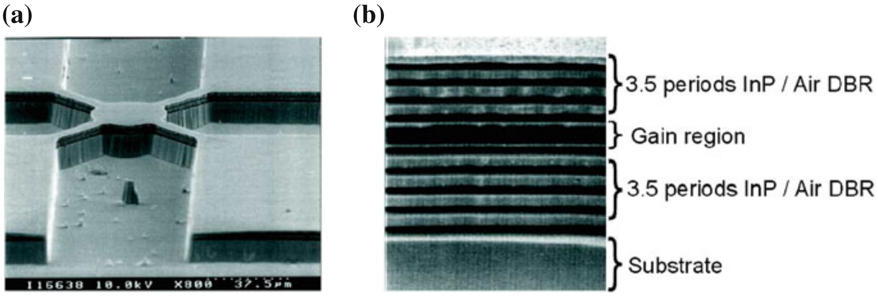

Fig. 23.71 (**a**) VCSEL with air gap and (**b**) Bragg mirror with high dielectric contrast InP/air interfaces. Reprinted with permission from [1724], © 2002 IEEE

23.4.15 Optically Pumped Semiconductor Lasers

An easy way to pump semiconductor lasers is optical pumping. This technique is similar to diode-pumped solid-state lasers (DPSS). A (semiconductor) pump diode illuminates a suitable semiconductor structure (Fig. 23.72). The resonator is built between the bottom Bragg mirror of the semiconductor and the output coupler. The semiconductor structure contains suitable absorption layers (barriers) that absorb the pump light and quantum wells that emit laser radiation. This radiation is intracavity frequency doubled. In order to reach, e.g., a 488 nm output laser beam, a standard 808 nm pump diode is employed. The InGaAs/GaAs quantum wells are designed to emit at 976 nm. Other design wavelengths of the quantum wells allow for other output wavelengths. This technology allows compact lasers with little heat dissipation [1725]. The optically pumped semiconductor laser (OPSL) is also known as a semiconductor disc laser.

23.4.16 Quantum Cascade Lasers

In a quantum cascade laser (QCL), the gain stems from an intersubband transition. The concept was conceived in 1971 [1729, 1730] and realized in 1994 [1676]. In Fig. 23.73a, the schematic conduction-band structure at operation is shown. The injector supplies electrons into the active region. The electron is removed quickly from the lower level in order to allow inversion. The electron is then extracted into the next injector. The laser medium consists of several such units as shown in Fig. 23.73b. Since every unit can deliver a photon per electron (with efficiency η_1), the total quantum efficiency of N units $\eta = N\,\eta_1$ can be larger than 1.

The emission wavelength is in the far- or mid-infrared, depending only on the designed layer thicknesses and *not* on the band gap of the material (Fig. 23.73d). In the mid-infrared, room-temperature operation has been achieved while operation in the far-infrared requires cooling so far. Extensions to the THz-range and the infrared spectral region (telecommunication wavelengths of 1.3 and 1.55 μm) seem feasible. The cascade laser concept can also be combined with the DFB technology to create single-mode laser emission (Fig. 23.73d).

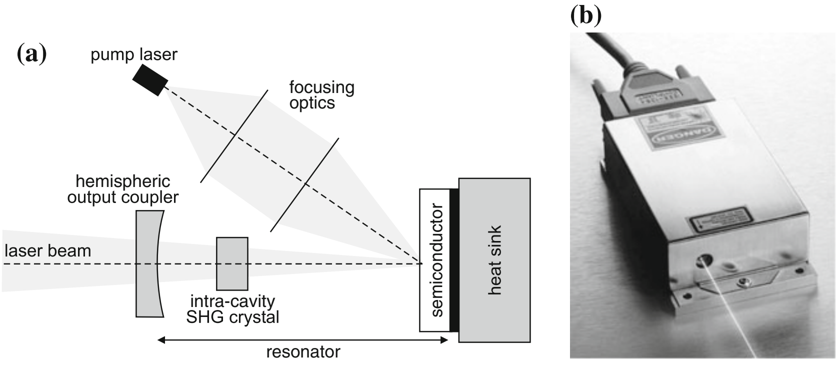

Fig. 23.72 (**a**) Schematic setup of optically pumped semiconductor laser (OPSL). The semiconductor chip consists of a Bragg mirror on the bottom, multiple quantum wells and an antireflection coating on the top. Adapted from [1725]. (**b**) OPSL source (488 nm, 20 mW, footprint: 125 × 70 mm^2). Reprinted with permission from [1726]

23.4.17 Hot-Hole Lasers

The hot-hole laser, which is mostly realized with p-doped Ge, is based on a population inversion between the light- and heavy-hole valence subbands. The laser operates with crossed electric and magnetic fields (Voigt configuration, typically $E = 0.5$–$3\,\mathrm{kV/cm}$, $B = 0.3$–$2\,\mathrm{T}$) and at cryogenic temperatures ($T = 4$–$40\,\mathrm{K}$) [1731–1733].

A significant scattering process of hot carriers is interaction with optical phonons, mainly optical phonon emission. This process has a threshold in carrier energy given by the optical phonon energy. For sufficiently high electric fields and at low temperature, hot carriers accelerate without acoustical phonon interaction (ballistic transport) along the crystallographic direction in which the electric field is applied. These hot carriers reach the optical phonon energy and lose all their energy due to emission

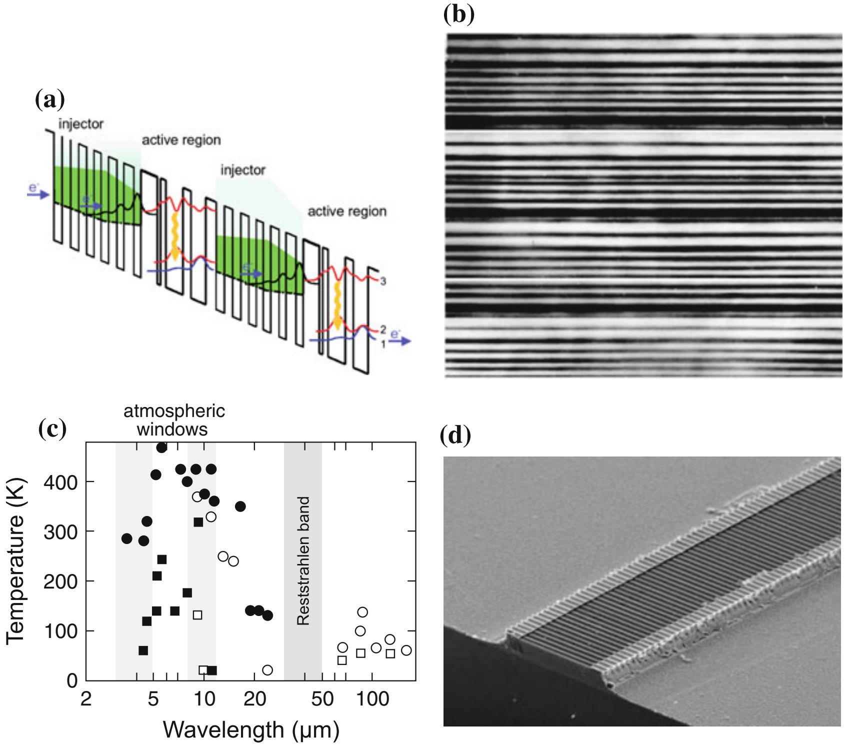

Fig. 23.73 (**a**) Schematic band diagram of quantum cascade laser. (**b**) Cross sectional TEM of cascade layer sequence. The periodicity of the vertical layer sequence is 45 nm. From [1727]. (**c**) Laser emission wavelengths and operation temperatures for various realized quantum cascade lasers (*squares*: cw, *circles*: pulsed operation, *solid symbols*: InP-, *empty symbols*: GaAs-based). Data from [1728]. (**d**) SEM image of a quantum cascade DFB laser (grating period: 1.6 μm). From [1728]

of an optical phonon. They accelerate again, repeating this directional motion in momentum space. This motion is called *streaming motion*.

For $|E/B|$ ratios of about 1.5 kV/cmT, the heavy holes are accelerated up to energies above the optical phonon energy (37 meV in germanium) and consequently are scattered strongly by these phonons. Under these conditions, a few per cent of the heavy holes are scattered into the light-hole band. The light holes remain at much lower energies and are accumulated at the bottom of the light-hole band below the optical phonon energy as sketched in Fig. 23.74. The continuous pumping of heavy holes into the light-hole band can lead to a population inversion. Consequently, laser radiation is emitted from optical (radiative) intervalence-band transitions (cf. Sect. 9.8.3). The emission wavelength is in the far-infrared around 100 μm. Typical p-Ge lasers span the frequency range 1–4 THz (300–70 μm) [1734] and deliver 1–10 W peak output power for 1 cm^3 typical active volume.

Since the applied electric field causes considerable heating, the temperature of the laser crystal rises quickly, within a few μs, up to 40 K. Then the laser action stops. Thus the duration of the electric-field excitation is limited to 1–5 μs (limiting the emission power) and the repetition frequency is only a few Hertz due to the necessary cooling. Research is underway towards high duty cycle (possibly cw) operation by using smaller volumes and planar vertical-cavities [1735, 1736].

23.5 Semiconductor Optical Amplifiers

If the facets of a laser cavity are antireflection coated, a laser gain medium can be used as a semiconductor optical amplifier (SOA). A textbook on this subject is [1737]. Optical feedback from facets can also be avoided using tilted facets [1738].

A tapered amplifier geometry, as shown in Fig. 23.75a, allows for laterally monomode input and a preservation of the lateral beam quality during the propagation of the optical wave through the gain medium. The active medium is an 8 nm compressively strained InGaAs quantum well. A typical taper angle is 5–10°.

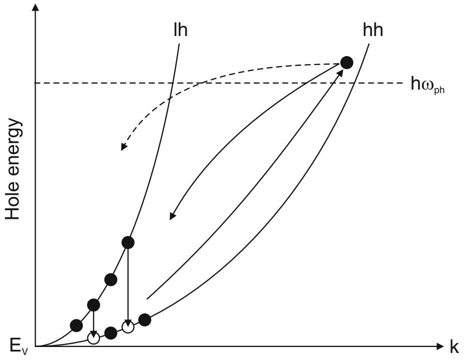

Fig. 23.74 Schematic cycle of hole motion in a hot-hole laser. *Filled* (*empty*) *circles* represent populated (unpopulated) hole states. The *solid lines* represent streaming motion of heavy hole, the *dashed line* represents scattering into the light hole band. *Arrows* denote radiative intervalence-band transitions

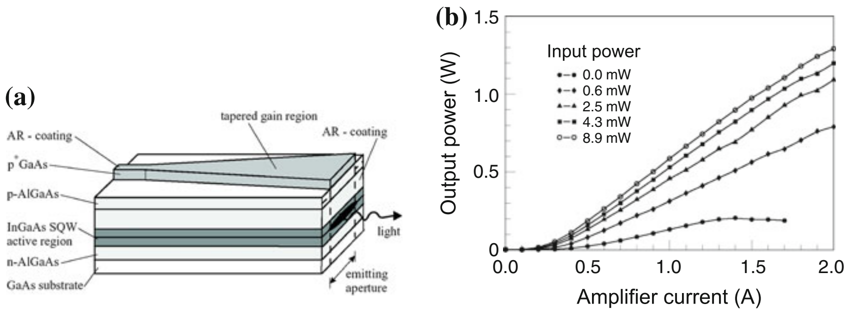

Fig. 23.75 (**a**) Schematic geometry of tapered semiconductor amplifier. (**b**) Optical output power versus amplifier current for various values of the optical input power, taper angle was 5°. For zero input power only spontaneous and amplified spontaneous emission is observed. Reprinted with permission from [1739]

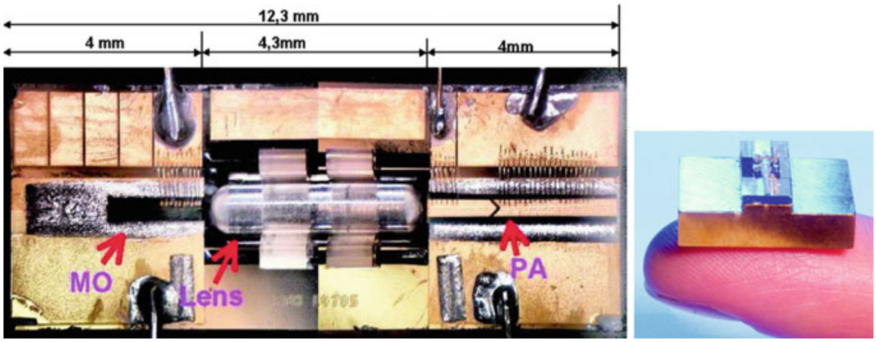

Fig. 23.76 Photographs of a MOPA arrangement of a laser (master oscillator, 'MO'), glass lens and tapered amplifier (power amplifier, 'PA') on a silicon micro-optical 'bench'. Reprinted with permission from [1740]

The input aperture is between 5 and 7 μm. The amplifier length is 2040 μm. More than 20 dB optical amplification can be obtained (Fig. 23.75b). The self-oscillation is suppressed for currents up to 2 A by AR facet coating of 10^{-4} in a 70 nm band. The wall-plug efficiency of the discussed amplifier is up to over 40 %. If such an amplifier is arranged together with a seed laser diode (master oscillator), the setup is called MOPA (master oscillator power amplifier), as shown in Fig. 23.76. A modulated input also leads to a modulated output.

Quantum dot arrays can be a useful gain medium in a SOA [1741, 1742] due to their fast gain dynamics [1743] and broad spectrum (Sect. 23.3.6).